144013 Tailored Assembly of 2D Heterostructures beyond Graphene

Kwang-Sup Lee
HANNAM UNIVERSITY

05/11/2017
Final Report

FORM SF 298

REPORT DOCUMENTATION PAGE

Form Approved
OMB No. 0704-0188

1. REPORT DATE *(DD-MM-YYYY)*	2. REPORT TYPE	3. DATES COVERED *(From - To)*
11-05-2017	Final	04 Jun 2014 to 03 Dec 2016

4. TITLE AND SUBTITLE
144013 Tailored Assembly of 2D Heterostructures beyond Graphene

5a. CONTRACT NUMBER

5b. GRANT NUMBER
FA2386-14-1-4013

5c. PROGRAM ELEMENT NUMBER
61102F

6. AUTHOR(S)
Kwang-Sup Lee

5d. PROJECT NUMBER

5e. TASK NUMBER

5f. WORK UNIT NUMBER

7. PERFORMING ORGANIZATION NAME(S) AND ADDRESS(ES)
HANNAM UNIVERSITY
70,HANNAM-RO DAEDEOK-GU,
DAEJEON, 306 - 791 KR

8. PERFORMING ORGANIZATION REPORT NUMBER

9. SPONSORING/MONITORING AGENCY NAME(S) AND ADDRESS(ES)
AOARD
UNIT 45002
APO AP 96338-5002

10. SPONSOR/MONITOR'S ACRONYM(S)
AFRL/AFOSR IOA

11. SPONSOR/MONITOR'S REPORT NUMBER(S)
AFRL-AFOSR-JP-TR-2017-0040

12. DISTRIBUTION/AVAILABILITY STATEMENT
A DISTRIBUTION UNLIMITED: PB Public Release

13. SUPPLEMENTARY NOTES

14. ABSTRACT

Rapid progress in graphene research has attracted further research attentions for other 2D layered materials. As the synthetic methods for 2D materials advance, a variety of functional heterostructures combined from these building blocks are attainable. Here we propose our synthetic approach to construct graphene-based 3D heterostructures composed of 2D layered materials with finely tunable morphology, structure, and functionalities. The resultant 3D composite materials are expected to possess unique set of synergistic functionalities that are hardly attainable in a single component material. We report selective CO_2 capture functionality of carbon nitride/graphene heterostructure, fundamental understanding of graphene oxide via rheology study, size-induced separation of large graphene oxide, and its potential functionalities in liquid crystal and catalyst application. Another important approach we have explored during this project is the solution phase assembly of two-dimensional materials through ligand mediated non-covalent interactions. This approach involves the synthesis of ligands, their self-assembly on two-dimensional materials as well as the use of such functionalized 2D materials to create 2D stacked structures.

15. SUBJECT TERMS
Nanotechnology

16. SECURITY CLASSIFICATION OF:			17. LIMITATION OF ABSTRACT	18. NUMBER OF PAGES	19a. NAME OF RESPONSIBLE PERSON
a. REPORT	b. ABSTRACT	c. THIS PAGE			CASTER, KENNETH
Unclassified	Unclassified	Unclassified	SAR	27	19b. TELEPHONE NUMBER *(Include area code)* 315-229-3326

AOARD Project Progress Report

(June 4, 2014 - September 3, 2016)

Title:

"Tailored Assembly of 2D Heterostructures beyond Graphene"

April 28, 2017

Principle Investigators

PI : Kwang-Sup Lee, Department of Advanced Materials, Hannam University, Daejeon, South Korea. Tel: +82-42-629-8857, Fax: +82-42-629-8853, E-mail: kslee@hnu.kr / kslee8857@gmail.com

Co-PI: Sang Ouk Kim, Department of Materials Science and Engineering, Korean Advanced Institute of Science and Technology (KAIST), Daejeon 305-701, South Korea. E-mail: sanouk.kim@kaist.ac.kr

Abstract

Rapid progress in graphene research has attracted further research attentions for other 2D layered materials. As the synthetic methods for 2D materials advance, a variety of functional heterostructures combined from these building blocks are attainable. Here we propose our synthetic approach to construct graphene-based 3D heterostructures composed of 2D layered materials with finely tunable morphology, structure, and functionalities. The resultant 3D composite materials are expected to possess unique set of synergistic functionalities that are hardly attainable in a single component material. We report selective CO_2 capture functionality of carbon nitride/graphene heterostructure, fundamental understanding of graphene oxide *via* rheology study, size-induced separation of large graphene oxide, and its potential functionalities in liquid crystal and catalyst application. Another important approach we have explored during this project is the solution phase assembly of two-dimensional materials through ligand mediated non-covalent interactions. This approach involves the synthesis of ligands, their self-assembly on two-dimensional materials as well as the use of such functionalized 2D materials to create 2D stacked structures.

Introduction

Discovery of graphene, which possess dramatically distinct properties from its stacked graphite form, has triggered tremendous research efforts for genuine 2D materials. As many scientists witnessed the exotic condensed matter physics of graphene, they naturally broaden their attention to other 2D layered materials, such as hexagonal boron nitride (h-BN), graphitic carbon nitrides (g-C_3N_4), and transition metal dichalcogenides (TMDCs) for diverse functionalities. To date, various synthetic methods for graphene have been established, including mechanical exfoliation, liquid phase exfoliation, and chemical vapor deposition, and opened up new opportunities to graphene based platform for novel heterostructures [1]. Synergistic interface between 2D layered materials and graphene may offer novel molecular tailored materials with advanced functionalities. Recent studies demonstrate several examples, including graphene/BN, graphene/MoS_2 for field-effect tunneling transistor [2], graphene/MoS_2 on TiO_2 nanoparticles for photocatalytic H_2 production [3], graphene/h-BN for flexible electronics/optics [4], and graphene/Zn-Cr-LDH 2D nanoplates for light induced O_2 production [5].

As physics has predicted exotic new phenomena in 2D materials and their nanohybrids, it has been a challenge for material scientists to achieve control of the properties of the 2D materials to attain desired material functionalities. The influences of molecular scale structure on the resultant material properties is clearly demonstrated by the apparent differences among carbon nanotubes, graphene, and fullerene on various properties including mechanical properties, band gap energy, electrical conductivity, carrier mobility, thermal conductivity, solution dispersibility, etc [6]. The assembly of graphene (and other carbon materials) into various 3D morphologies is of great research interest due to its wide impact on potential applications including energy harvest/storage, catalysis, sensors, and display [7-9]. Nevertheless, controlling the molecular scale structures of graphene is challenging due to its inherent strong tendency for interlayer π-π stacking, which renders graphitic stacking with minimal surface area [7,10]. Novel 3D assembly strategies, such as gelation, layer-by-layer assembly, and interfacial heterostructure growth, can be exploited to overcome inherent tendency of graphitic stacking and to obtain macroscopic functional graphene based materials with high electrical conductivity, high surface area, soft and hydrated surface with potential

modification capability [11-13]. Similar molecular scale assembly approaches also offers convenient and straightforward route to various graphene based 3D heterostructures with dynamic arrays of potential functionalities.

This work done during the performance period of this project involved various strategies to achieve assembly of graphene, or other 2D materials and explore their applications. The milestones of this project are summarized as follows:

1. Synthesis, characterization and study of ligands with conjugated molecule end-functionalization for coupling graphene sheets.
2. Establishment and optimization of graphene gel synthesis for maximized functional group incorporation and idealized porosity.
3. Characterization of porous structure using N_2 isotherm, BET surface area, TEM, SEM, and adjust reaction parameter to obtain desired porous architecture.
4. Crosslinking desired 2D layer building blocks (C_3N_4, $MoSe_2$, WSe_2, etc) with graphene sheet while maintaining porous structure by controlling various reaction parameters such as pH, concentration, temperature, pressure, solvent, and aging time.
5. Solution phase assembly of graphene-transition metal dichalcogenides heterostructures.

Experiment

Synthesis of Ligands: The proposed synthesis of ligands for non-covalent coupling of nanomaterials to graphene has been successfully accomplished. The scheme for synthesis of ligands can be seen in Figure 1(a). The ligands constitute a thiol group at one and the aromatic pyrene moiety at the other. The pyrene moiety interacts with 2D materials like graphene through its highly conjugated electron rich structure. The thiol group at the other end meanwhile can interact with quantum dots as well as suitable 2D materials. The possible interaction of the ligands in coupling graphene sheets to quantum dots and the 2D materials WSe_2 can be seen in Figure 1 (b)-(c). The ligands differ only by their spacer lengths. PyTh ligands with n= 4, 6, 10 will mentioned to as PyTh4, PyTh6 and PyTh10 from here onwards. The spacer lengths of PyTh4, PyTh6 and PyTh10 are 8.6 Å, 10.7 Å and 17.7 Å, respectively.

Synthesis of Carbon Nitride Functionalized Aerogel: L-Ascorbic acid (0.1 g) and varying amounts of dicyanamide (40-400 mg) were added to 5 mL of exfoliated graphene oxide solution (2.4 mg·mL^{-1}) and heated with stirring at 50 °C for 30 min. The resulting black solution was cooled to room temperature, and slow gelation occurred within 8-10 hr, turning the viscous solution into a monolithic gel. This gel was first washed with hot H_2O twice and then submerged with H_2O for 5 days and ethanol for 5 days, consecutively. Every 8 hr, submerging solvent medium was exchanged with fresh medium to wash out remaining ionic precursors or by products. Solvent-exchanged gel is dried with CO_2 at supercritical point. The resulting gel turns into a flexible and monolithic aerogel. The monolithic D-rGA sample was placed inside of a ceramic crucible and heated in the tubular furnace under nitrogen atmosphere at 200 °C for 2 hr. The ramping rate was set to 5 °C/min, and cooling was performed at room temperature quenching.

Synthesis of Size-Selected Large Graphene Oxide: Graphene oxide (GO) is prepared by a modified Hummers method. For the size selection of large flakes, the GO solution was

diluted to 0.2 mg/mL and placed at room temperature for 1-2 week. After complete phase separation, the top isotropic phase was gently removed by pipetting. To prepare small GO, an large GO solution was sonicated for 2 h.

N-doping and Reduction of Graphene Oxide: For the N-doping and reduction of GO, a 0.5 mg/mL GO solution was freeze-dried. The obtained GO aerogel was placed in a hydrazine vapor filled chamber for 1 hr at 90 °C and thermally reduced at 750 °C under a H_2 (60 sccm) and NH_3 (40 sccm) atmosphere.

Synthesis of Pristine and Iron (Fe^{2+})-Functionalized Carbon Nitride: Dicyandiamide (1 g) was ground with mortar and pestle. For iron-functionalized carbon nitride samples, a corresponding amount of iron halide was added (12.6 mg of $Fe(II)Cl_2$) and ground spontaneously. Ground dicyandiamide (with or without halide iron) was placed inside a ceramic crucible and put into furnace chamber. The crucible was heated in the furnace under nitrogen blowing environment at a rate of 2.5 K·min^{-1} for 4 h to reach 600 °C and another 4 h of heating at that temperature. Crucible was naturally quenched, and sample was collected after cooling.

Electrochemical Analysis: Catalyst ink was prepared by mixing 1 mg of N-doped reduced GO (N-rGO) aerogel, 800 μL of a 2-propanol–water mixture (1:3 v/v) (Sigma-Aldrich), and 21 μL of 5 wt % Nafion (Sigma-Aldrich), which was further sonicated for 30 min for stable dispersion. For the preparation of the Pt/C electrode, 5 mg of Pt/C and 16 μL of 5 wt % Nafion were mixed with 4 mL of a 2-propanol–water mixture and sonicated for 30 min. Finally, 10 μL of the ink was dropped on the glassy carbon rotating disc electrode of 5 mm diameter, which had been polished with alumina paste and cleaned by sonication. Cyclic voltammetry, linear sweep voltammograms, and chronoamperometry were performed in a three-electrode electrochemical cell, consisting of a Pt wire as a counter electrode and Ag/AgCl as a reference electrode. The electrolyte was 0.1 M KOH.

CO$_2$ and N$_2$ Adsorption Analysis: Before the gas adsorption measurement, reduced graphene oxide (rGO) aerogel samples were dried under vacuum at 200 °C for 24 hr. For gas adsorption, Micromeritics ASAP 2020 was used to evaluate how effective these rGO aerogel samples can adsorb CO_2 gas in comparison with N_2 gas. CO_2 and N_2 gas adsorption/ desorption isotherms were measured in the range of 0-1 bar at 300 K separately. For regenerability evaluation experiments, multiple runs of CO_2 adsorption isotherm were measured without degassing process before the analysis.

Photocatalytic Activity: The photocatalytic activity of the g-C_3N_4 and Fe-g-C_3N_4 were evaluated in terms of the degradation of p-nitrophenol (PNP) under sunlight irradiation. For photocatalytic measurements, the sample was suspended in 10 ppm PNP solution, and the solution is kept under stirring under pH 9 condition. Prior to irradiation, the suspension is magnetically stirred under dark condition for about 1 hr to ensure the complete establishment of an adsorption–desorption equilibrium. The sample was irradiated using Xe lamp (Newport Co., Ltd., Model 66984) at a power of 300 W. The decrease in absorbance of a certain characteristic peak of PNP was measured at regular intervals using UV-vis spectroscopy (Varian Cary5000 UV-vis-NIR spectrophotometer). Band gap energy shift was estimated based on absorption coefficient (α), Planck constant ($\hbar$), light frequency (ν), band gap energy (E_g), and a constant (A).

$$\alpha \hbar \nu = A(\hbar \nu - E_g)^{n/2}$$

Measurements: For structural analysis, NMR (Bruker AVANCE 400WB) is used to identify the bonding position of multivalent iron ion in carbon nitride network and was checked for ^{13}C and ^{15}N nuclei, especially size distributions of GO flakes data were measured with Inspector 2.1 software. Raman spectroscopy was carried out with ARAMIS. FT-IR spectroscopy was measured using Bruker IF66/S and Hyperioin 3000 with attenuated total reflectance (ATR) mode between 600 and 4000 cm^{-1}. Powder X-ray diffraction (PXRD) analysis was performed using Rigaku D/MAX-2500 (18 kW) within 3-60° range, 2°/min scan speed, and 40 kV 300 mA. X-ray photoelectron spectroscopy (XPS) measurement was performed using Thermo VG Scientific Sigma Probe. The CHN element was analyzed using a Thermo Scientific Flash 2000 analyzer. Scanning electron microscope (SEM) images were taken using FEI Magellan 400 with 1-5 kV power, 13 pA to 1.6 nA current, and 500×-100000× magnification mode. Transmission electron microscope (TEM) images were captured using FEI Tecnai G2 F30. Thermal gravimetric analysis was performed by Setaram Setsys 16/18 at 25-600 °C in N$_2$ atmosphere. Detailed analysis of porous structures was determined through nitrogen and argon adsorption/desorption isotherm. Micromeritics ASAP 2020 was used for both N$_2$ and Ar isotherm measurement. Brunauer-Emmett-Teller (BET) and Horvath-Kawazoe (HK) models were used to evaluate surface area and pore size distribution, respectively. All electrochemical performance was measured by a Bio-Logic SAS SP-200 model. Absorption spectra of samples were measured by UV-vis spectroscopy (JASCO, V530, Japan).

Results and Discussion

1. Synthesis, characterization and study of ligands with conjugated molecule end-functionalization for coupling graphene sheets.

The ligands were synthesized as described in the experimental section. The scheme for synthesis of ligands can be seen in Figure 1(a). The ligands constitute a thiol group at one and the aromatic pyrene moiety at the other. The pyrene moiety interacts with 2D materials like graphene through its highly conjugated electron rich structure. The thiol group at the other end meanwhile can interact with quantum dots as well as suitable 2D materials. The possible interaction of the ligands in coupling graphene sheets to quantum dots and the 2D materials WSe$_2$ can be seen in Figure 1(b)-(c). The ligands differ only by their spacer lengths. PyTh ligands with n= 4, 6, 10 will mentioned to as PyTh4, PyTh6 and PyTh10 from here onwards. The spacer lengths of PyTh4, PyTh6 and PyTh10 are 8.6, 10.7, and 17.7 Å, respectively.

Coupling QDs with Graphene Sheets: Coupling QDs functionalized by PyTh ligands to graphene is essentially process of self-assembly. The nanoparticles and graphene are dispersed in same or miscible solvents. The two materials are brought gradual mixing. An ideal experiment involves a dilute dispersion of graphenic material to which the functionalized QDs are added in small quantities over a period of time followed by sonication. The concentration of the functionalized QDs should also be kept low so as to avoid aggregation between nanoparticles. There are many ways to synthesize graphene which includes micromechanical exfoliation of graphite, chemical vapour deposition, epitaxial growth on electrically insulating surface, liquid phase and electrochemical exfoliation of graphite and graphite intercalation compounds, chemical reduction of graphene oxide or graphite oxide, etc [14]. We tested three different types of grapheme sources in our

experiments namely (i) electrochemical exfoliation of highly oriented pyrolytic graphite (HOPG) [15], (ii) reduction of graphene oxide by phenyl hydrazine, and (iii) graphene nanoplatelets stabilized by graphene oxide [16].
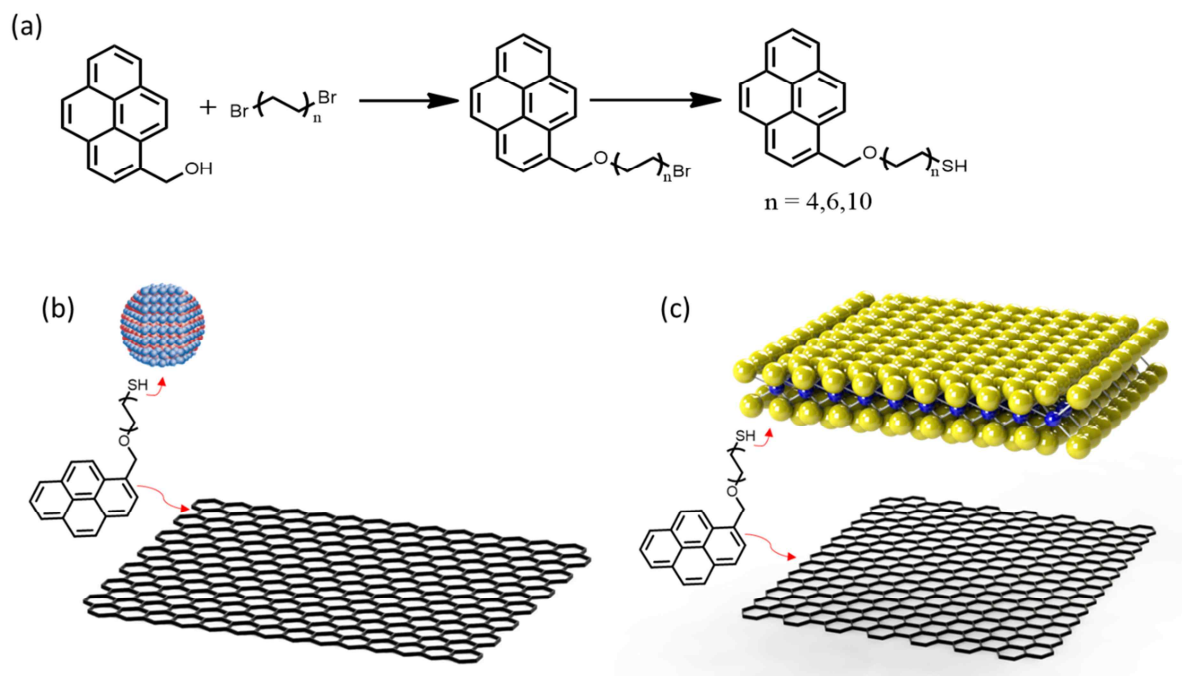

Figure 1. (a) The scheme for synthesis of PyTh ligands of different spacer lengths, (b) non-covalent coupling of QDs with graphene, and (c) non-covalent coupling of WSe_2 with graphene

GO-GNP paper: Graphene nanoplatelets (GNPs) stabilized by graphene oxide (GO) prepared by following the previously reported procedures [16-17]. GNPs provide the intrinsic graphene electrical conductivity to the GNP/GO films. The GNP/GO film was ultrasonicated in NMP for 1 hr, and centrifuged to obtain a stable dispersion of GNP/GO sheets. The synthesis of GNP/GO is summarized in Figure 2.

Chemically Converted Graphene: Graphene oxide is chemically reduced into graphene (CCG) with phenyl hydrazine in room temperature. The CCG is redispersed in NMP by ultrasonication for 1 hr. The chemical procedure for synthesis of CCG is given in Figure 3.

Electrochemically Exfoilated Graphene: Graphene sheets are obtained from electrochemical exfoliation of highly oriented pyrolytic graphite (HOPG) flake. Two electrode system containing platinum as counter electrode and HOPG as working electrode is employed with aqueous H_2SO_4 electrolyte. When a direct current voltage is applied to HOPG electrode, the HOPG flakes starts to exfoliate and disperse into electrolyte solution. On completion of exfoliation process, the exfoliated graphene sheets are collected by vacuum filtration and repeatedly washed away any residual salts. The collected exfoliated graphene are further ultrasonicated in NMP, and centrifuged to remove any unexfoliated products. The well

dispersed and stable graphene sheets in NMP are collected. The chemical procedure for synthesis of electrochemically exfoliated grapheme is given in Figure 4 [17].
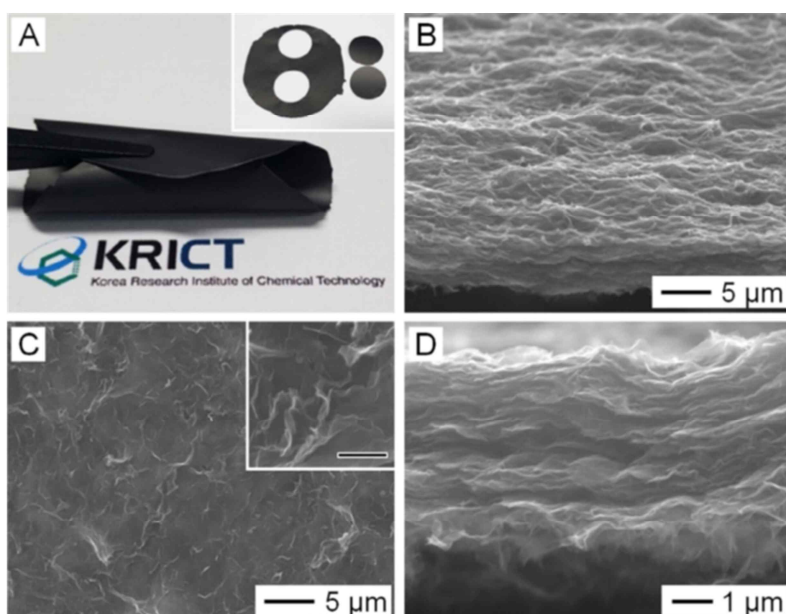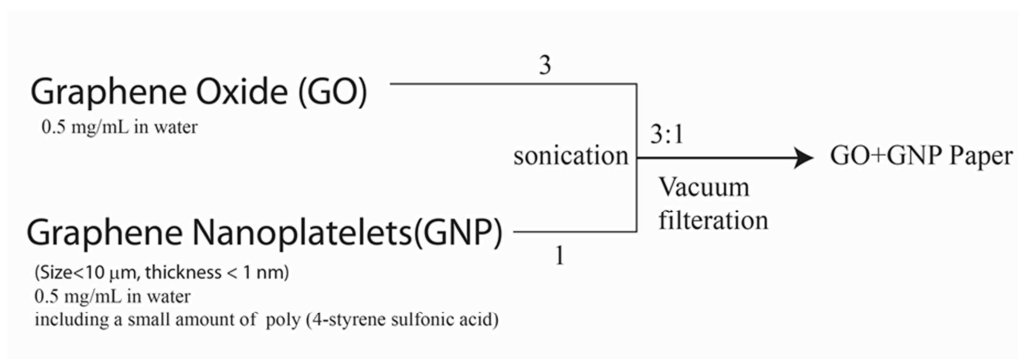

Figure 2. Procedure for GO-GNP paper preparation (a) photograph of GO+GNP paper (b) tilted view (c) top view (d) cross-sectional view
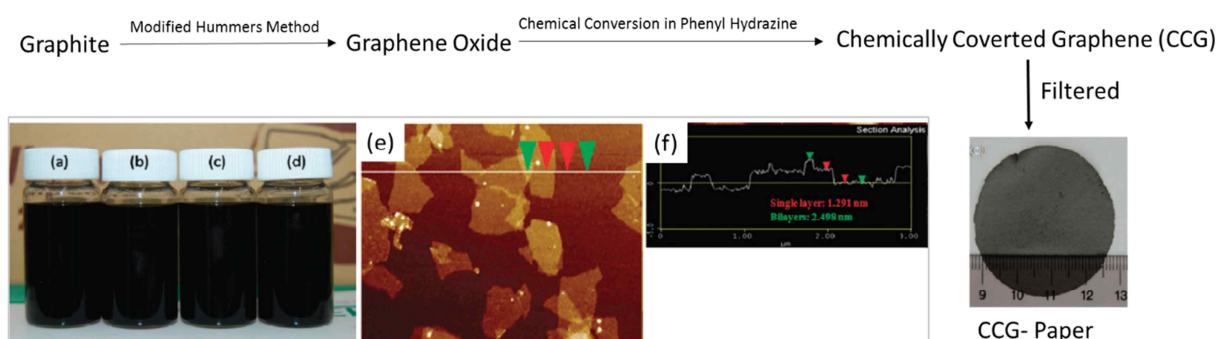

Figure 3. Preparation of chemically converted graphene (CCG) (a)-(d) *N,N'*-dimethylacetamide (DMAc), *N,N'*-dimethylformamide (DMF), propylene carbonate (PC), and 1-methyl-2-pyrrolidinone (NMP), (e) AFM image

CCG-paper sheet, (f) Corresponding AFM line profile the arrows in (f) indicate where line profiles were measured. The height of profile shows the presence of few layer CCG flakes.
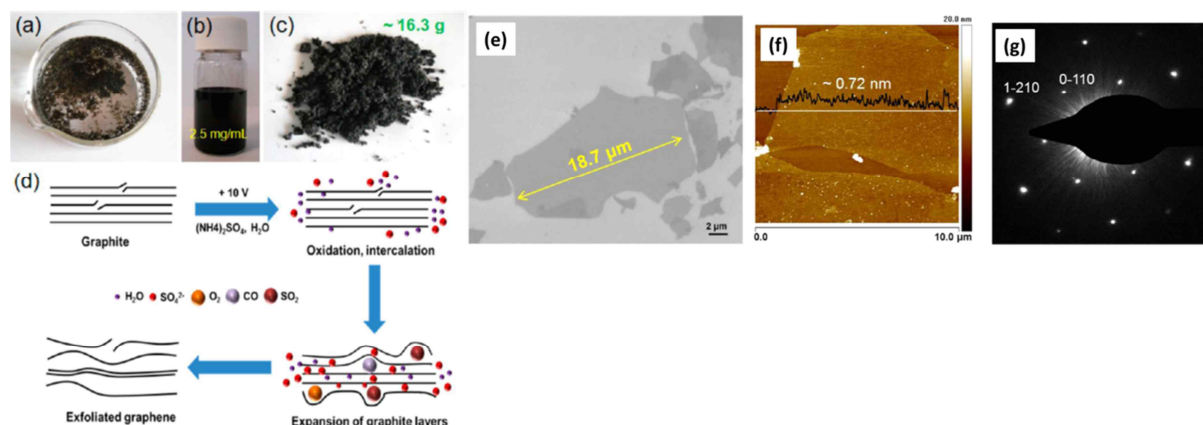

Figure 4. (a) Graphite flakes after electrochemical exfoliation. (b) Dispersed EEG in DMF solution (concentration ~2.5 mg/mL). (c) EG powders on a bulk scale. (d) Schematic illustration of the mechanism of electrochemical exfoliation (Graphite Anode, Pt Cathode). (e) TEM image of EEG. (F) AFM image of EEG on silicon substrate. (g) SAED pattern

Coupling QDs with PyTh Ligands: Of the three different types of graphene sources, the electrochemically exfoliated graphene (EEG) was found to be most suitable for the self-assembly of materials because of its larger size and the fewer number of layers. Cadmium selenide-zinc sulfide (CdSe-ZnS) core-shell QDs were synthesized by following the literature methods [18]. At the end of the nanoparticle synthesis oleic acid coupled QDs are obtained. These nanoparticles can be precipitated by centrifugation at 4,000 rpm for 6 min, followed by decantation of the supernatant. The nanoparticle can be dispersed by adding chloroform ($CHCl_3$) and sonicating for 10 min. Ligand exchange with PyTh can be carried out in chloroform. The oleic acid ligands on QDs can be replaced by PyTh ligands by a simple sonication procedure carried out in $CHCl_3$. A ligand solution (15 mg/20 ml $CHCl_3$) was added dropwise to the QD dispersion while sonicating the mixture for an hour. The excess ligand was removed by centrifugation leading to precipitation of the functionalized QDs. The supernatant was drained and QDs were re-dissolved in $CHCl_3$ and the washing procedure was repeated 5-6 times.

Coupling QD-PyTh with EEG: To couple graphene with the PyTh functionalized QDs, the centrifugate from QD functionalization was dispersed in chloroform and N_2 gas was bubbled through the dispersion and 1 mg of graphene dispersed in *N*-methyl-2-pyrrolidone was added to this dispersion and sonicated for 1 hr. After this the QD-graphene hybrid was separated by centrifugation. It can be dispersed in chloroform with 2-3 drops of toluene. This dispersion was used for TEM images. The results from the TEM experiments are summarized in Figure 5. The self-assembly of QDs functionalized with PyTh4 ligand can be seen in Figure 5(a-c), similarly results from QD-PyTh6-EEG and QD-PyTh10-EEG can be seen in Figure 5(d-f) and Figure 5(g-i), respectively. Closer examination of TEM images in QD-PyTh-EEG samples reveals an even coverage of nanoparticles on EEG sheets. There are lighter regions of uniform particle distribution as well as darker regions in the TEM images feature small aggregates of nanoparticles. These aggregates can be clearly seen in the higher resolution images in Figure 5(c,f,i). There is a potential to achieve a much more uniform distribution of nanoparticles over graphene by careful control over the mixing of nanoparticles and

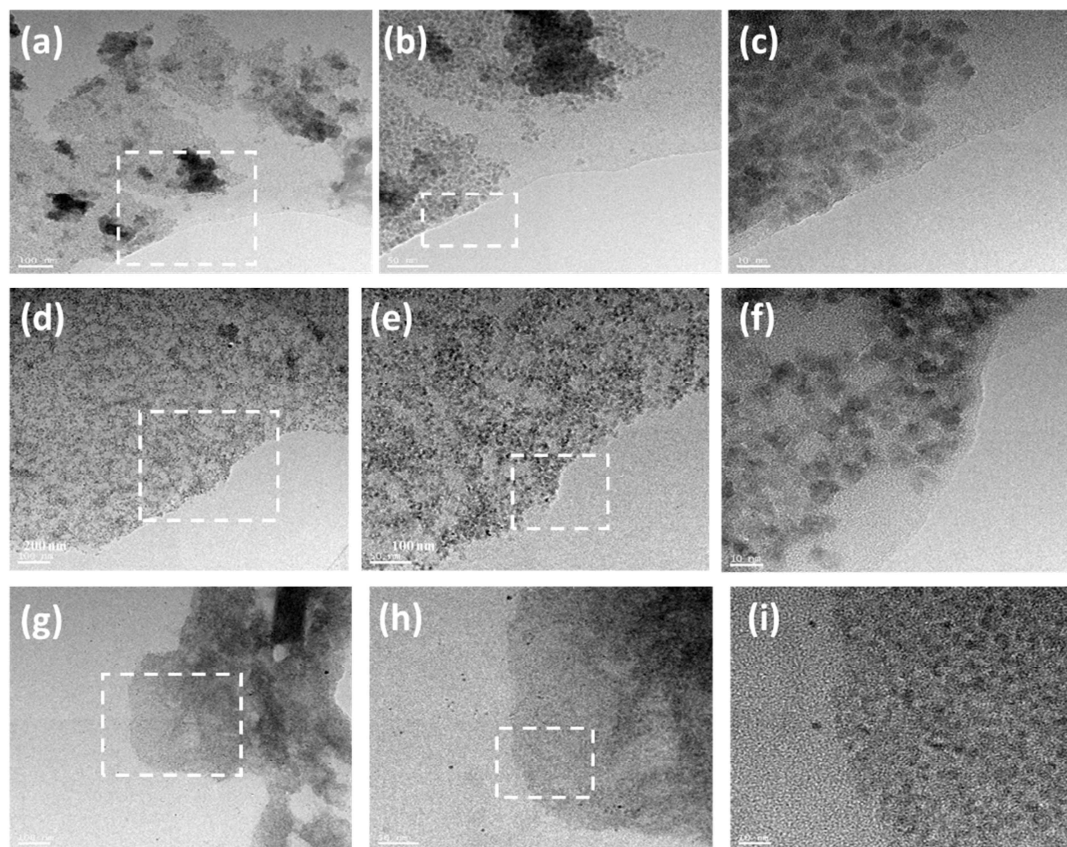optimizing the nucleation growth of the nanoparticle.

Figure 5. TEM images of QD-PyTh-G nanohybrids from ligands with different spacer lengths: (a)-(c) QD-PyTh4-G, (d)-(f) QD-PyTh6-G, and (g)-(i) QD-PyTh10-G. The open rectangles in the first two images in every row roughly indicating the area imaged in the following figure. The scaled bars for the figures in each row are from left to right 200 nm, 50 nm and 10 nm, respectively.

Absorption and Emission Properties of Quantum dot Graphene Hybrids: The steady state absorption and fluorescence of the QD-PyTh-EEG samples can be seen in Figure 6. The absorption spectra of featuring ligands can be seen in Figure 6(a,c,e). Each of the graphs contains UV-vis spectra of the ligands (PyTh4, PyTh6 and PyTh10), QD-functionalized with the ligands (PyTh4-QD, PyTh6-QD and PyTh10-QD), and the graphene-coupled systems (QD-PyTh4-EEG, QD-PyTh6-EEG, QD-PyTh10-EEG). The functionalization of the ligand onto the nanoparticle and then the functionalization of the nanoparticle on to graphene can be tracked by looking at the high energy pyrene peak around 325 nm-350 nm. The features in this region of the spectrum can see in the ligand functionalized QD (PyTh-QD) given in red as well as the QD-PyTh-EEG samples given in blue. The red lines in the emission spectrum are a combination of the absorption of the QDs as well as the pyrene ligands. The general shape of the spectrum is different for the pure ligand, the ligand functionalized QD as well as the graphene-QD nanohybrids. This shows that energy levels of the materials are changing with their functionalization. The photoluminescence studies summarized in Figure 6(b,d,f). The photoluminescence intensity follows the trend PyTh> QD-PyTh> QD-PyTh-EEG for all three ligands. The decrease in intensity of the PL peaks in QD-PyTh-EEG is an indicator of energy or electron transfer interactions between the QD and EEG.
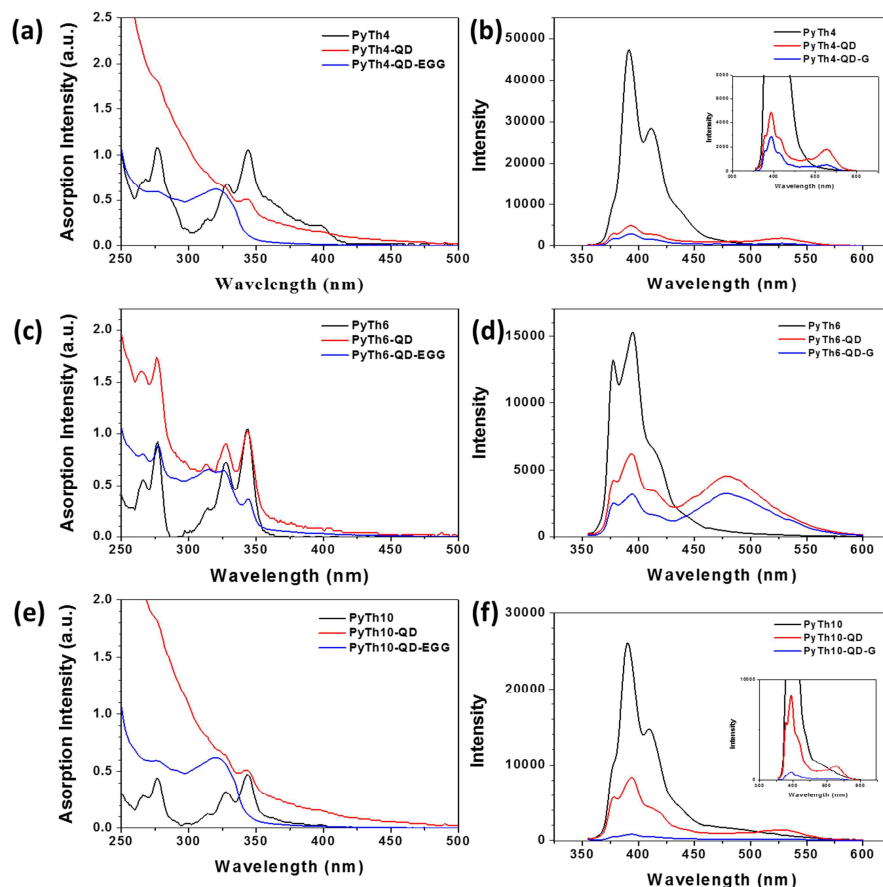
Figure 6. (a)-(b) absorption-emission spectra of PyTh4, QD-PyTh4 and QD-PyTh4-EEG, (d) -(c) absorption-emission spectra of PyTh6, QD-PyTh6 and QD-PyTh6-EEG and (e)-(f) PyTh10, QD-PyTh10 and QD-PyTh10-EEG.

Energy Transfer in Quantum dot Graphene Hybrids by Confocal Photoluminescence: The energy transfer in QD-PyTh-EEG was further inverstigated using laser confocal microscopy photoluminescence (LCM-PL) experiments. These experiments allow the characterization of photoluminescence at a microscopic region of the sample. The QD-PyTh as well as the QD-PyTh-EEG samples was casted onto a slide glass and they were studied using confocal fluorescence microscopy. The graphs in Figure 7(a,c,e) show the LCM-PL measurements on QD-PyTh4, QD-PyTh6 and QD-PyTh10 samples, respectively. The inset in the graphs show the flouresence map of the sample, the curves represent the PL spectra of the QD-PyTh sample measured at different points indicated by numbers in the inset. The PL spectra from LCM-PL unlike the steady state PL discussed above shows higher intensity for QD fluorescence at 517 nm compared to fluorescence of the pyrene moiety around 410 nm. The LCM-PL spectra of the QD-PyTh4-EEG, QD-PyTh6-EEG and QD-PyTh10-EEG are given in Figure 7(b,d,f). The PL spectrum features PL peaks of both pyrene and QDs. Currently there is some hardware limitation in LCM-PL for studying the whole of the floresencent spectrum of QD-PyTh-EEG which ranges from 350-600 nm in Figure 6(b,d,f). We are trying to have the broadest wavelength window in this range to understand the dynamics of energy transfer in these hybrids. The variation in local concentration of the nanohybrid can influence the intensities seen in the LCM-PL measurements. Hence to have a better idea about the

excited state dynamics of the QD-PyTh-EEG hybrids time resolved PL (trPL) were carried out.
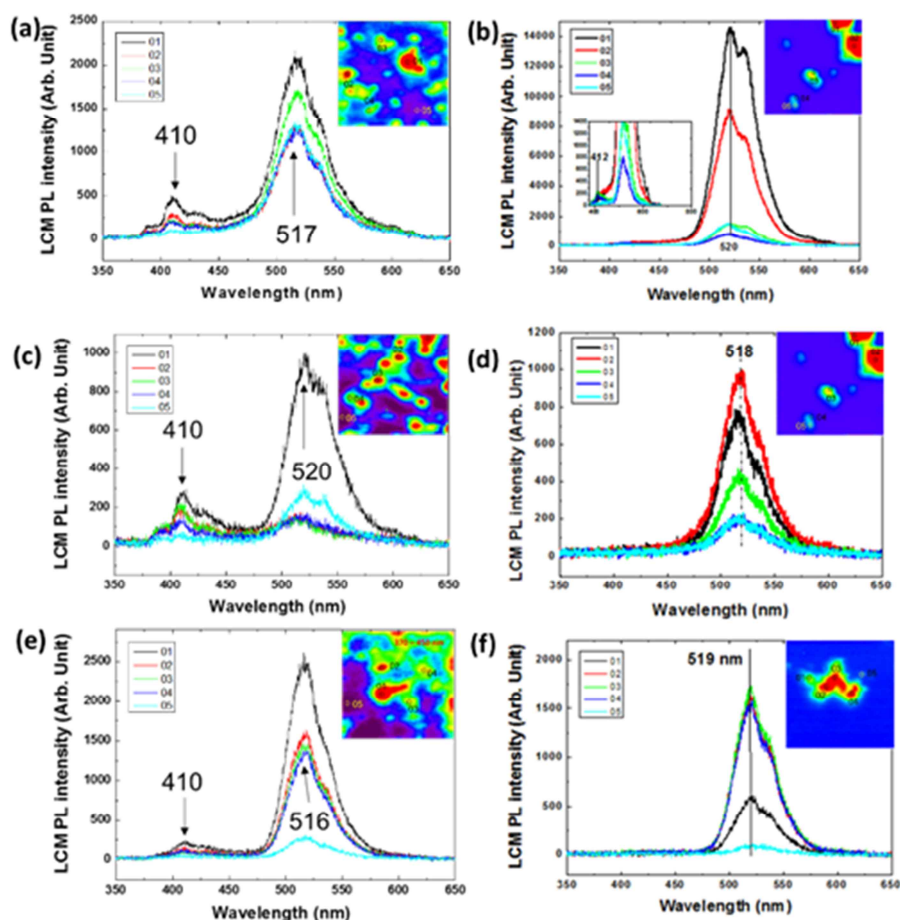

Figure 7. Photoluminescence spectra of the PyTh-QD samples with those of QD-PyTh-EEG samples. Figure (a), (c) and (e) shows the PL measurement done on five different spots on a drop cast sample of PyTh4, PyTh6 and PyTh10, respectively. Insets of the graphs show the PL mapping of the sample surface signifying the varying PL intensities in different positions on the sample. The measure spots are indicated by number in the inset. Figure(b), (d) and (f) represent the LCM-PL fluorescence peak as well as the fluorescence intensity mapping of QD-PyTh4-G, QD-PyTh6-G, QD-PyTh10-G, respectively.

Energy Transfer in Quantum dot Graphene Hybrids by Time Resolved Photoluminescence:
Time resolved PL (Tr-PL) experiments allow the study of time dependent decay of fluorescence excitation. A decrease in fluorescence life time between of the QDs in QD-PyTh-EEG compared to that in QD-PyTh is an indicator of energy or electron transfer between the QD and graphene (Figure 8). Pyrene has been known to form charge-seperated excited states when coupled with gold nanoparticles. This means that pyrene in the excited state interacts with gold nanoparticles through electron transfer rather than energy transfer [19]. Further it has been shown that in pyrene end functionalized alkyl thiols and amines show erratic emissive behavior when functionalized on gold nanoparticles because of complex factors governing the interaction between the excited pyrene moiety.
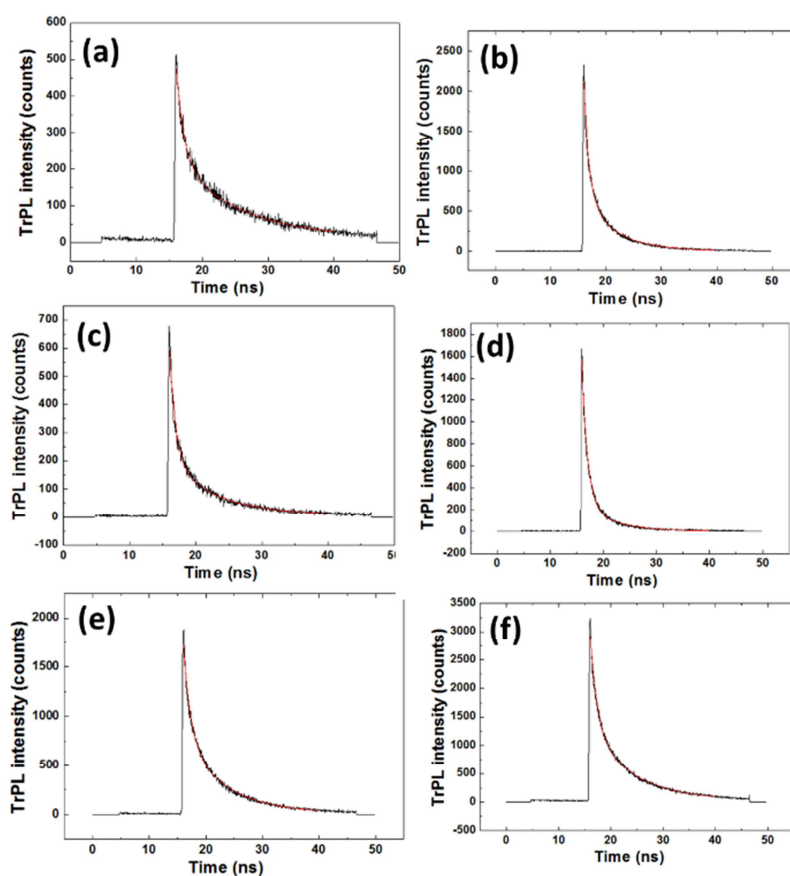
Figure 8. Time resolved PL measurements on QD-PyTh and QD-PyTh-EEG. (a) QD-PyTh4, (b) QD-PyTh4-EEG, (c) QD-PyTh6, (d) QD-PyTh6-EEG, (c) QD-PyTh10, (d) QD-PyTh10-EEG.

One of the main factors governing the interaction pyerene and the nanoparticle surface is the angle between the surface of the nanoparticle and the pyrene moiety. In case of gold nanoparticles functionalized with thiol-alkyl-pyrene ligands it was established that the π-interactions between pyrene functional groups govern the arrangement of ligands. For longer alkyl chains the interaction between the alkyl chains rather than pyrene drive the assembly and configuration of ligands on the nanoparticle [20]. The different driving factor in the short and long chain ligands result in different electron transfer interactions with the surface of the nanoparticle. The shorter ligand has the pyrene oriented almost perpendicular to the surface of the nanoparticle while the longer ligand results in a more acute angle. The electronic interaction between the pyrene in the excited state and the nanoparticle are governed by the overlap of energy levels as well as the electric field generated by the nanoparticle. The orientation of the pyrene ligands from the short chains will minimize overlap with the energy levels of the nanoparticle leading to inefficient quenching of fluorescence. This tendency can be viewed in Table 1 which summarizes the results from the TrPL experiments. The shorter ligand functionalized PyTh4-QD has the longest average excited state life time (τ_{avg}) of 5.06 ns, consequently when this QD is coupled with EEG the nanohybrid shows a τ_{avg} of 2.45 ns. The difference in fluorescence lifetimes of PyTh4-QD and PyTh4-QD-EEG, $\Delta\tau$ is 2.61 ns. This means that the quenching takes place in 2.61 ns. For the longer chain PyTh6-QD PL is quenched at 2.19 ns, which is shorter than PyTh4-QD. This is in keeping with the observation for pyrene functionalized gold surfaces [20]. When PyTh6-QD is functionalized on graphene

the PyTh6-QD-EEG nanohybrid shows a fluorescence life time of 1.83 ns. The value of $\Delta\tau$=0.38 ns which is much shorter than in the case of PyTh4-QD-EEG. Surprisingly in the case of the longest ligand coupled with QD, QD-PyTh10 the fluorescence life again increases to 3.91 ns. This can only be explained by the increasing distance between the pyrene and QD. The same explanation can be used for the longer fluorescence life time of QD-PyTh10-EEG which is 4.29 ns. This means that functionalization with graphene stabilizes the fluorescence of the PyTh-QD. We are currently studying these systems in detail to explain the observed trends. The observation of longer life time in the case of longest chains may be due to carried recombination effects arising from inefficient electron transfer between QD-PyTh10 and EEG [21]. To conclude the QD-PyTh-EEG nanohybrids have unique energy transfer behavior based on their spacer length. This understanding is being applied for the fabrication of new optoelectronic devices.

Table 1. Summarizes the results from QD-PyTh ligands and their graphene hybrids

Component	Spacer Length (Å)[a]	τ_{avg} (ns)[b]	$\Delta\tau$[c]
QD-PyTh4	8.6	5.06	
QD-PyTh4-EEG	-	2.45	2.61
QD-PyTh6	10.7	2.19	
QD-PyTh6-EEG	-	1.83	0.36
QD-PyTh10	17.7	3.91	
QD-PyTh10-EEG		4.29	-0.38

[a]The spacing length of the ligand measured from the pyrene-alkyl chain bond to the thiol group at the end of the thiol group, [b]the fluorescence lifetime in nanosecond measured from TrPL experiments, [c]The difference in fluorescence lifetime between QD-PyTh and its corresponding QD-PyTh-EEG

Heterostructure Assembly of Graphene and Tungsten Diselenide (WSe₂): Layered two dimensional materials such as graphene or transition metal dichalcogenides are of considerable interest as potential electronic materials for future electronics [22]. However the practical application of these materials are restricted by their intrinsic limitations such as absence of band gap in graphene and low electron mobility in transition metal dichalcogenides like WSe_2. Assembling graphene and WSe_2 in vertical heterostructures enables the synergic combination of their properties. Many device applications such as high-electron-mobility transistors, lasers, light-emitting diodes, solar cells, photodetector, supercapacitor, and catalysis can be realized by such heterostructures [23]. The solution phase synthesis of such heterostructures requires specific ligands to direct the vertical self-assembly. Here, we investigate solution phase synthesis of graphene-WSe_2 heterostructures through thiol terminated pyrene containing ligands (PyTh). The schematic of ligand synthesis is given in Figure 9. A straight forward heterostructure assembly of graphene and WSe_2 is possible in the solution phase by the utilization of these ligands, as demonstrated by a high-resolution SEM and TEM images Figure 9(a,b), respectively. The direct visualization of

graphene and WSe$_2$ domains enabled by the elemental mapping as shown in Figure 9(c-f), confirms the successful formation of graphene-WSe$_2$ heterostructure.
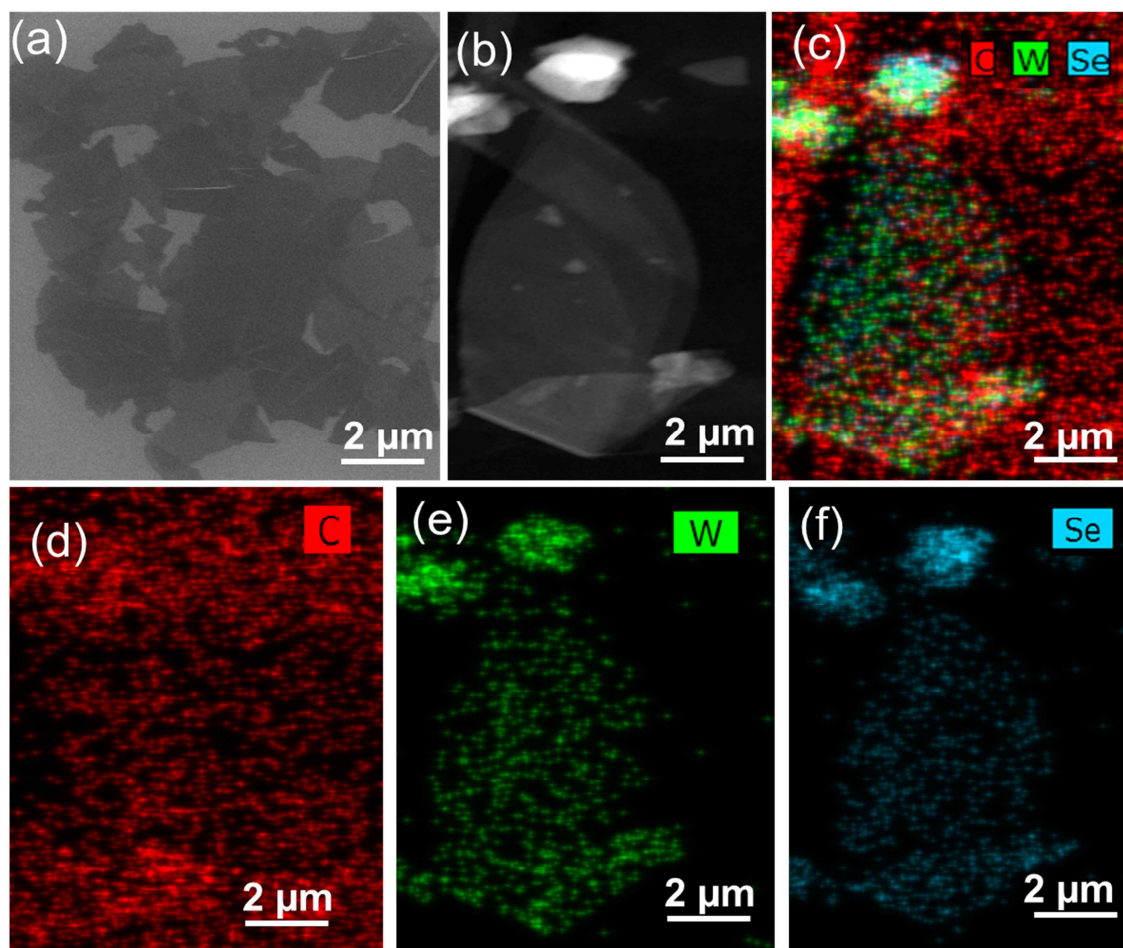

Figure 9. (a) SEM analysis of graphene-WSe$_2$ heterostructure. (b) TEM image, and (c-f) elemental mapping of graphene-WSe2 heterostructure.

2. Carbon Nitride Functionalized Graphene Aerogel

We have achieved proposed milestones regarding the synthesis, optimization, and application of graphene based 3D heterostructure [24]. We investigated how various factors of sol-gel synthesis of reduced graphene oxide can deliver stable porous structure with efficient CO$_2$ capture functionality. Further, we have investigated the effect of various physical parameters (e.g. temperature, concentration, solvent, reducing agent) on self-assembly of chemically exfoliated graphene oxide solution, and systematically observed the effect of nitrogen functionalization on CO$_2$ capture functionality of resulting graphene material. Three dimensional porous framework of amorphous carbon nitride functionalized graphene aerogel (CN-GA) is constructed through modified graphene oxide gelation principle. Resulting materials exploits both porous graphene backbones which readily introduce incoming gas molecule and stably supports carbon nitride groups, and carbon nitride sites capable of reversible CO$_2$ capture through favorable binding energy and mutually oriented adsorption sites as seen in Figure 10.
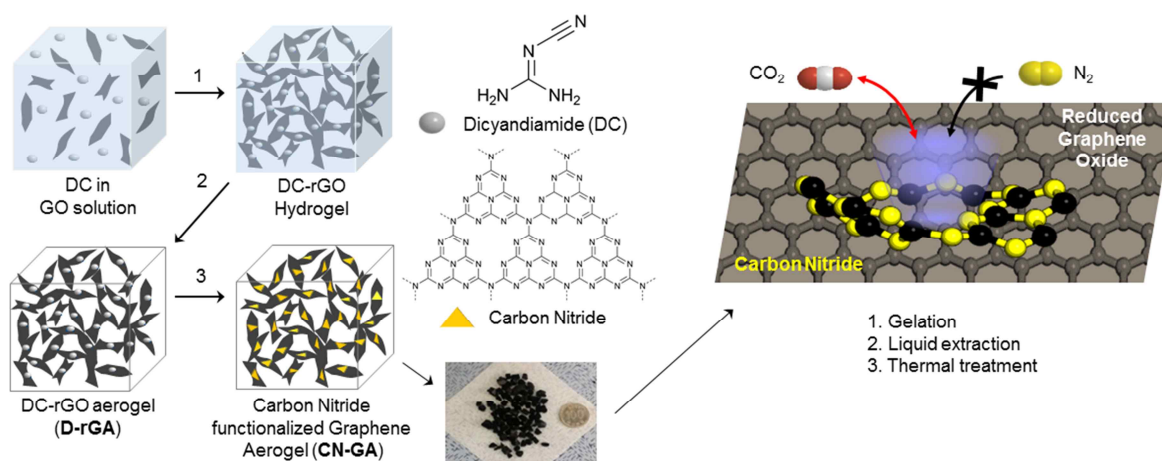
Figure 10. Carbon nitride (g-C_3N_4) functionalized graphene aerogel (CN-GA) synthesis

This amorphous carbon nitride groups provides effective CO_2 adsorption functionality. Although pristine graphene oxide aerogel itself possess intrinsic adsorption capacity, incremental nitrogen content and thermal treatment have beneficial impact on CO_2 capture functionality. Pristine reduced graphene oxide aerogel (rGA) show 0.9 mmol·g^{-1} adsorption capacity at standard ambient temperature and pressure (SATP, 300K and 1 bar) whereas dicyandiamide decorated graphene aerogel (D-rGA) show enhanced CO_2 uptakes of 2.2 mmol·g^{-1} at SATP as seen in Figure 11(a). Carbon nitride graphene aerogel (CN-GA) possess even superior CO_2 adsorption capacity of 4.2 mmol·g^{-1} at SATP surpassing those of other existing carbon based adsorbents. This enhancement of CO_2 adsorption capacity demonstrate pivotal role of carbon nitride sites in anchoring CO_2.
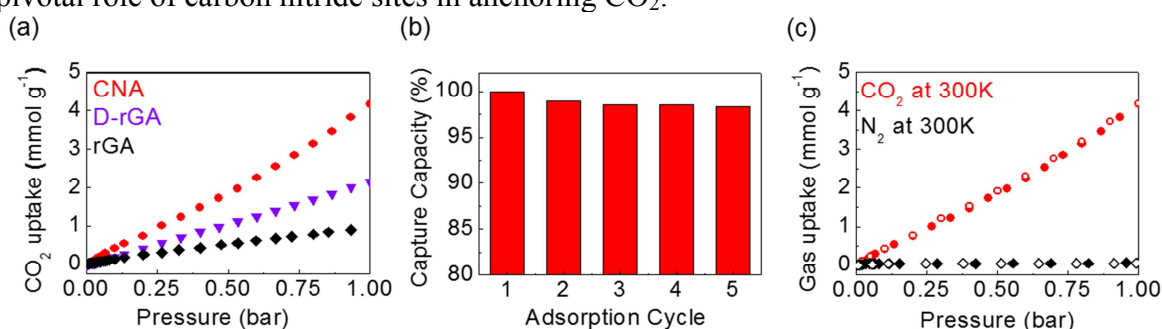

Figure 11. (a) CO_2 adsorption isotherms of carbon nitride graphene aerogel (CN-GA), dicyandiamide functionalized reduced graphene oxide aerogel (D-rGA) at various contents of nitrogen (3-8%), and pristine reduced graphene oxide aerogel (rGA). (b) Multiple cycles of relative CO_2 adsorption capacity for regenerability test for CN-GA at 1 bar. (c) CO_2 and N_2 adsorption isotherms of CN-GA with high selectivity toward CO_2.

The CO_2 sequestration capability of CN-GA is compared with well-known bench mark materials in terms of five adsorbent criteria: CO_2 adsorption capacity (N_1^{ads} [mmol·g^{-1}]), working capacity ($\Delta N_1 = N_1^{ads} - N_1^{des}$ [mmol·g^{-1}]), regenerability (R = ($\Delta N_1/N_1^{ads}$) × 100 [%]), adsorption selectivity ($\alpha_{12}^{ads} = (N_1^{ads}/N_2^{ads})(y_2/y_1)$), and sorbent selection parameter (S = $(\alpha_{12}^{ads})^2(\alpha_{12}^{des})(\Delta N_1/\Delta N_2)$) [25-28]. Adsorption and desorption pressures were chosen at 0.1 bar and 0.01 bar, respectively. The CO_2 adsorption properties of CN-GA and benchmark

materials are summarized in Table 2. Since CO_2 exists as a minor phase (approximately 10-15%) in flue gas, adsorption capacity at 0.1 bar is appropriate to evaluate practical CO_2 adsorption efficiency from flue gas. CN-GA shows moderate N_1^{ads} value of 0.43 mmol·g^{-1} compared to strong binding adsorbents, such as Zeolite-5A (3.50 mmol·g^{-1}), and Ni-MOF-74 (4.34 mmol·g^{-1}). The adsorption capacity reflects the binding strength at adsorbent surface.

Table 2. The CO_2 adsorption property of CN-GA and benchmark materials

	N_1^{ads}	ΔN_1	R	α_{12}^{ads}	S
ZIF-78 [29]	0.60	0.58	96	35	396
Zeolite-5A [30]	3.50	2.36	67	62	163
Ni-MOF-74 [27]	4.34	3.20	74	41	84
Co MOF-4b	0.07	0.06	84	154	104
rGA	0.14	0.13	93	39	175
CN-GA	0.43	0.42	98	113	427

N_1^{ads} [mmol g^{-1}] : CO_2 uptake under adsorption conditions / $\Delta N_1 = N_1^{ads} - N_1^{des}$ [mmol g^{-1}] : Working CO_2 capacity / R = $(\Delta N_1/N_1^{ads})$ * 100 [%] : Regenerability / $\alpha_{12}^{ads} = (N_1^{ads}/N_2^{ads})(y_2/y_1)$: Selectivity under ambient adsorption conditions / S = $(\alpha_{12}^{ads})^2/(\alpha_{12}^{des})(\Delta N_1/\Delta N_2)$: Sorbent selection parameter / 1 : strongly adsorbed component (CO_2) / 2 : weakly adsorbed component (N_2) / y : molar fraction in the equilibrium gas phase

The effective CO_2 adsorption of CN-GA at ambient condition with moderate adsorption strength is beneficial for facile regeneration by pressure driven CO_2 adsorption/desorption (vacuum swing adsorption. Working capacity (ΔN_1), net amount of CO_2 release after adsorption, and regenerability (R), the percentage of reusable CO_2 capture site, reflect this aspect. Adsorbents with strong chemisorption sites generally suffer from largely diminished working capacity with respect to initial adsorption capacity, as demonstrated in Zeolite-5A (2.36 mmol·g^{-1} / 3.50 mmol·g^{-1}), and Ni-MOF-74 (3.20 mmol·g^{-1} / 4.34 mmol·g^{-1}). By contrast, mild adsorbents such as ZIF-78 (0.58 mmol·g^{-1} / 0.60 mmol·g^{-1}), and CN-GA (0.42 mmol·g^{-1} / 0.43 mmol·g^{-1}) show minor reduction of working capacity. Notably, CN-GA exhibits an excellent regenerability of 97.6%. The CO_2 adsorption/desorption isotherms for repeated cycles (Figure 11(b)) also show regenerability higher than 90% even after 5 cycles. Interestingly, unlike other moderate binding adsorbents such as ZIF-78, CN-GA exhibits highly selective CO_2 adsorption against abundant N_2, as demonstrated by selectivity parameter (α_{12}^{ads}) and experimental adsorption result (Figure 11(c)). The CO_2 and N_2 adsorption/desorption isotherms at 300 K reveals an outstanding selectivity value of 113. It is noteworthy that metal-free CN-GA system displays equivalent or even higher selectivity over other candidates. Significantly, sorbent selection parameter (S) is the key criterion, which sums up all aspects of adsorption/desorption capacity and selectivity. It represents overall performance of adsorbent in a given condition. CN-GA shows the highest S value of 427 among all benchmark candidates (Table 2). Taken together, these evaluation results indicate the great advantages of carbon nitride adsorbent for practical flue gas treatment, particularly in terms of regenerability and selectivity, which rarely coexist.

3. Rheological Properties of Graphene Oxide Liquid Crystal

We report the rheological properties of liquid crystalline graphene oxide (GO) aqueous dispersion. GO dispersions exhibit typical shear thinning behaviors of liquid crystals, which is described by power law or simple Curreau model [31]. Irrespective of the shear rate, shear viscosity exhibits sudden decrease with the increase of GO composition around a critical volume fraction, $\phi_c = 0.33\%$, demonstrating typical colloidal isotropic-nematic phase transition. Dynamic measurements reveal the liquid-like (isotropic phase, $G' > G''$) behavior at a low GO composition ($\phi \sim 0.08\%$) and solid-like (liquid crystalline) behavior at higher compositions ($\phi \sim 0.45\%$), where G' exceeds over G''. Nematic gel-like phase is confirmed at a higher GO composition over $\phi > 0.83\%$, where both G' and G'' moduli are nearly independent of frequency (ω). Simple power law scaling arguments are introduced to model the dependence of yield stress and viscoelastic moduli on the GO composition. We also observed the yield stress and rigidity percolation transition above phase transition composition $\phi_c > 0.33\%$ with a percolation exponent of 1.3 ± 0.1. These rheological insights provide valuable information for the liquid crystalline processing of GO based materials including fibers, sheets and other complex structures for electronic/optoelectronic and energy storage/conversion applications.

Figure 12(a) shows the SEM image of as-synthesized GO platelets with the mean lateral size of ~ 700 nm. AFM image of GO sheets with a height profile is shown in Figure 12(b), which confirms the monolayer thickness of ~ 1 nm. The structure and properties of GO dispersions are strongly dependent on the interactions between the platelets. The steric hindrance from overlapping of GO platelets arises at high composition, results in configurational entropy driven excluded-volume effects [32]. Well-known Onsager's model accounts for the formation of nematic liquid crystals based on purely entropy-driven mechanism [33]. The thermodynamic equilibrium liquid crystal phase originates from the competition between orientational and positional entropies. In dilute dispersion, the orientational entropy is maximized due to random orientation of GO platelets. By contrast, above critical GO concentration, the GO platelets orientate parallel to each other in order to minimize the excluded volume of the approaching platelets. Thus, the parallel arrangement of anisotropic GO platelets maximizes the packing or positional entropy that governs the formation of nematic liquid crystalline GO dispersions. The liquid crystalline phase can be easily identified from polarized optical microscopy. GO dispersions does not show any optical birefringence at low volume fraction, $\phi \sim 0.08\%$. Biphasic dispersion is observed between 0.15% and 0.45%. Entire nematic phase is confirmed above a volume fraction of 0.45%. Typical optical birefringent texture of single nematic LC phase for $\phi \sim 0.45\%$ is shown in Figure 12(c). This birefringence texture indicates the characteristic of anisotropic phases originates from the alignment of anisotropic platelets. The liquid crystalline GO dispersions are further confirmed from freeze-dried sample. Aqueous dispersion of $\phi = 0.45\%$ quenched in liquid N_2 and subsequently freeze-dried. The freeze-dried sample was subjected to SEM observation. Figure 12(d) clearly demonstrates the ordered GO platelets in the nematic phase.

Molecular ordering is particularly significant in the systems of anisotropic colloidal particles, polymers or worm-like micelles, where external shear can readily induce alignment and orientational order. To understand the orientational behavior of GO dispersions under shear, steady state shear flow curves were measured. Figure 13(a) shows the evolution of shear
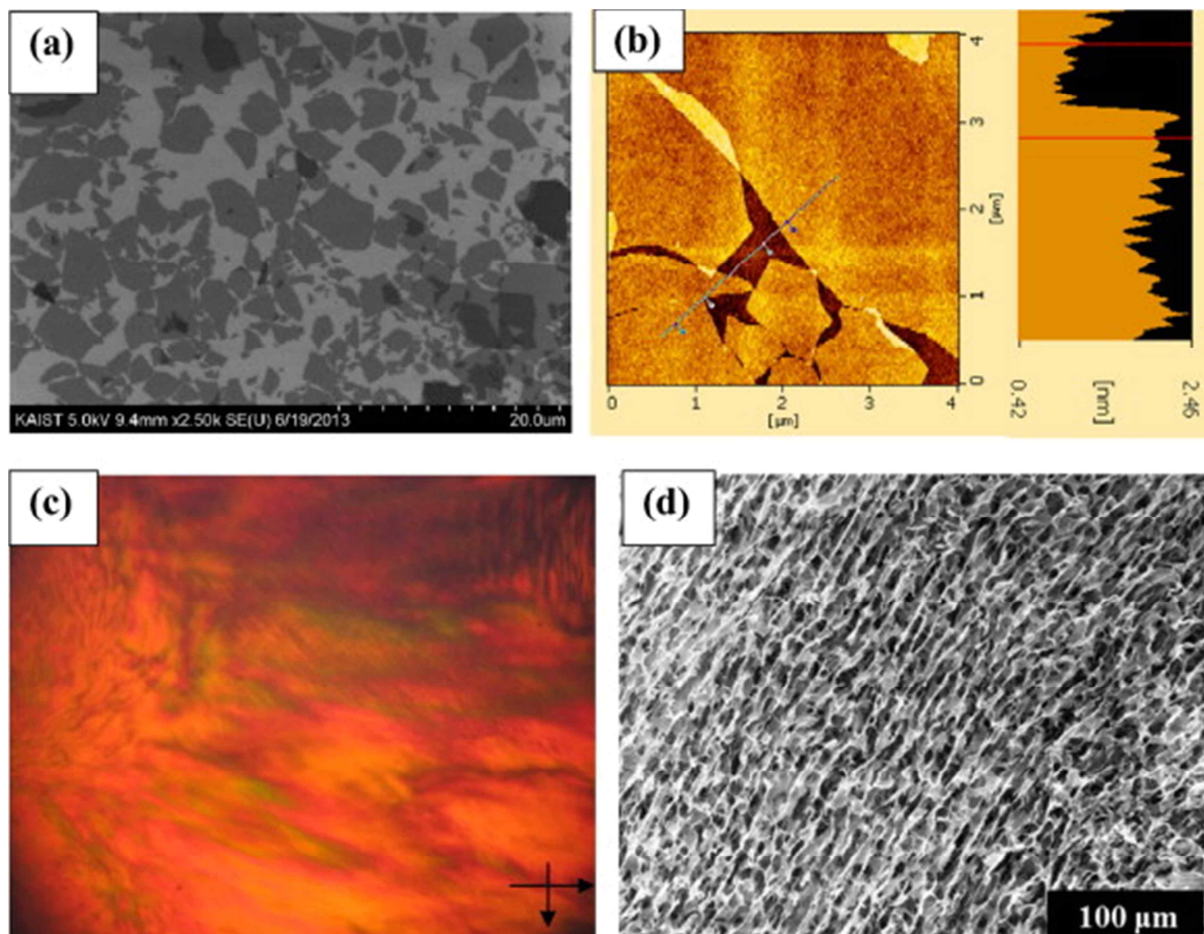
Figure 12. (a) SEM image of synthesized GO flakes deposited on Si substrate. (b) AFM image of GO sheets with height profile showing the typical monolayer thickness of ~1 nm. (c) Polarized light microscopy of GO aqueous dispersion showing optically birefringent texture. (d) Freeze dried SEM image of GO liquid crystalline phase.
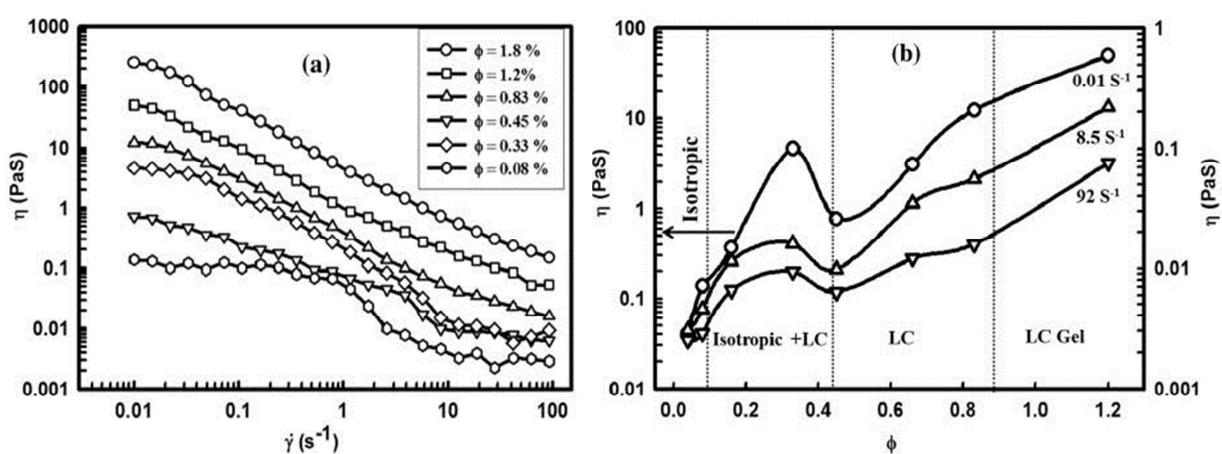

Figure 13. (a) Evolution of shear viscosity with shear rate at different GO composition. (b) Non-monotonic constitutive relation between shear viscosity vs GO composition demonstrating isotropic to nematic phase transition.

viscosity against shear rate for various GO compositions. GO dispersion exhibits Newtonian and non-Newtonian (shear thinning) behavior strongly depend on the ϕ. At low $\phi = 0.08\%$, shear viscosity shows Newtonian behavior at low and high shear rate with a shear thinning region at intermediate range. At a high GO composition, GO dispersion exhibits typical shear thinning behaviors. Moreover, the viscosity is found to show non-monotonic behavior with composition, which will be discussed later. Observed shear thinning is associated to the orientation of GO platelets in nematic dispersion. The flow behavior can be approximated by power law and Curreau shear thinning models. In power law shear thinning behavior ($\eta \approx \gamma^{x-1}$) with η the viscosity, k a constant, the shear rate and x the power law exponent [34]. The exponent $x = 1$ is retrieved for Newtonian flow and $x < 1$ is for shear thinning fluids. In Figure 13(a), we have fitted the power law in the low shear rate regime (0.01–1 s^{-1}). The exponents, x decrease from 0.9 to 0.29 with volume fraction. The exponent, $x = 0.9$ matches well with the one for isotropic dispersion at $\phi = 0.08\%$ with Newtonian behavior, while $x = 0.29$ for $\phi = 1.8\%$ corresponds the typical values of weak gels or concentrated dispersions. The shear thinning over the entire shear rate range can be also described by the simple Curreau equation [35],

$$\eta(\gamma) \approx \eta(\gamma \to 0)/[1+(\tau_r\gamma)^2]^m, \eta(\gamma) \approx \eta(\gamma \to 0)/[1+(\tau r\gamma)2]m,$$

where m, and τ_r define the shear thinning exponent and orientational relaxation time in the system, respectively. We find that shear thinning exponent of $m = 0.38$ for $\phi = 0.08\%$, is close to liquid-like (isotropic) behavior. By contrast, exponent, $m = 0.61$ for $\phi = 1.8$ close to highly entangled polymer melts and concentrated solutions [36]. Moreover, relaxation time, τ_r increase from 4.5 to 45 s when ϕ increase from 0.08% to 1.8%. This increase in relaxation time of GO platelets should manifest the maximization of packing and enhanced orientation of GO platelets along the shear direction.

Viscosity behavior of liquid crystalline dispersions depends not only on the GO composition but also on molecular arrangements in the dispersion. Figure 13(b) shows the evolution of shear viscosity with volume fraction, ϕ for shear rates of 0.01, 8.5, and 92 s^{-1}. Interestingly, viscosity exhibits non-monotonic behavior with increasing ϕ. At a low fraction of $\Phi = 0.08$, GO dispersion is in isotropic phase. Afterwards, viscosity increased up to a critical fraction ($\phi_c \sim 0.33$) and get maxima. With the further increase in ϕ_c, viscosity goes down and exhibits minima before increasing again. This viscosity reduction above a critical volume fraction, $\phi_c \sim 0.33$, is caused by the formation of low-viscosity nematic liquid crystalline phase. The viscosity minima approximately correspond to the GO composition for entire nematic phase formation. The transition from isotropic to nematic phase can be observed for the GO composition range between the maxima and minima in shear viscosity. In this work, $\phi_c = 0.33\%$ is considered as the critical GO composition for isotropic–nematic phase transition, which is close to theoretical predicated value (0.25%) for polydispersed infinitely thin platelets [37]. We note that this GO liquid crystal phase transition behavior agrees well with our previous optical characterization with polarized optical microscopy [38].

4. Selective Separation of Large Graphene Oxide in Liquid Crystal Phase

We have investigated a simple size-selection method taking advantage of liquid crystalline properties induced phase separation [39]. Application of graphene oxide in various field have critically limited on GO flake size. Top-down approach causes oxygen functionalities and

defects at flake edges and those defects have been highlighted as obstacles to reduce electrical and mechanical properties of GO based materials. Therefore, utilizing larger size of graphene oxide with lower edge ratio has been highly demanded. However, random oxidation reaction and exfoliation leads to broad size distribution of GO flakes. In this research, we achieved a novel size selection method by using its liquid crystalline behavior. A GO dispersion was prepared by a modified Hummers method and exfoliation by mild shaking.
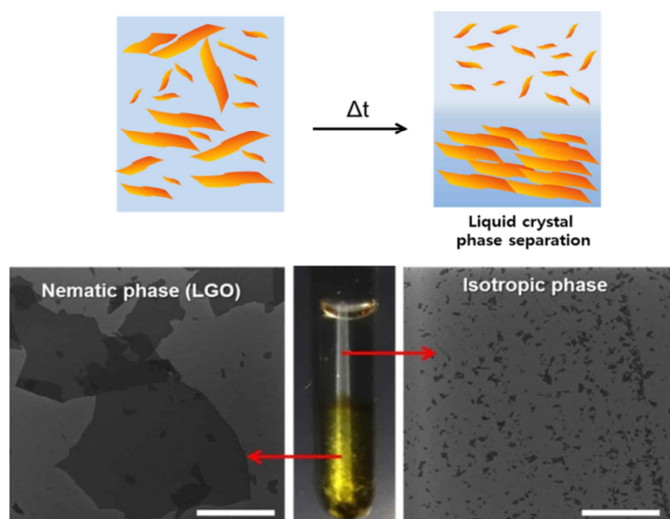

Figure 14. Spontaneous phase separation of GO aqueous solution and its composition

Ionic impurities, which decrease solubility of GO by screening the electrostatic repulsive force, were removed by filtration and dialysis. After then, GO dispersion was spontaneously phase-separated in specific concentration range (Figure 14). Between two cross-polarizers, distinguishable bright color and brushes were observed only in the bottom phase, and it implies the formation of isotropic-nematic binary phase. The composition of each phase were observed by SEM. Small GO (SGO) flakes are concentrated in the upper isotropic phase while large GO (LGO) flakes are concentrated bottom nematic phase. Removal of upper nematic phase enables simple separation of LGO and repeated fractionation is also possible. Figure 15 shows dominant 90% weight fraction of LGO (>20um) compared to 70% value of original solution.
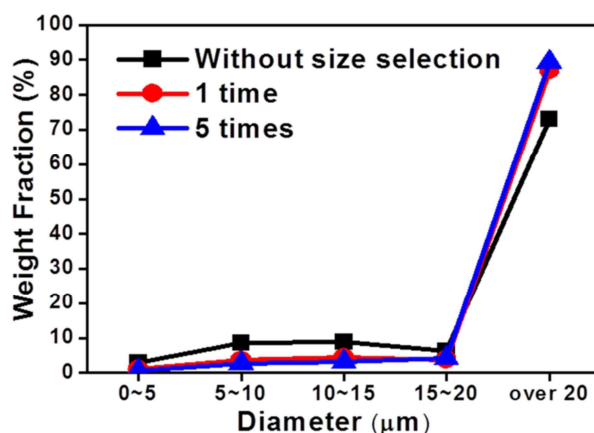

Figure 15. Statistical diameter distributions of GO after size fraction.

We further investigated influence of flake size on the substitutional nitrogen-doping (Figure 16). Small GO (SGO) and large GO (LGO) aerogel was reduced by hydrazine vapor and subsequent thermal annealing in H_2/NH_3 atmosphere. In Figure 16(b), N 1s peak of XPS analysis shows different nitrogen doping phenomenon in each GO. N-rSGO which has abundant edge shows dominant pyridinic peaks (N_P) while it rapidly decreases in quaternary (N_Q) dominant N-rLGO. The first report on the catalytic oxygen reduction reaction (ORR) of N-doped graphene has been controversial [40]. Both N_P and N_Q have been suggested as a catalytic center which adsorbs and reduces oxygen, but experimental and theoretical studies have been inconsistent. Thus, we analyzed ORR activities of each N-rSGO and N-rLGO from Figure 16(c-e). In cyclic voltammetry, both N-doped graphene shows distinct ORR peaks at (-0.4V) only in oxygen saturated 0.1M KOH electrolyte. In linear sweep voltammograms, the onset potential positively shifted in N-rLGO (-0.08 V) compared to N_P dominant N-rSGO (-0.11 V). Electron transfer number calculated from the slope of a Koutechy-Levich plot shows remarkable 4-electron reduction pathway in the case of N-rLGO. However, N-rSGO exhibits 2.5 electron transfer pathway in same condition. Our experimental results are highly consistent with theoretical studies that lone electron pairs in N_P repel oxygen molecules while N_Q dopants gives catalytic activities to neighboring carbon atoms by leading partial plus charge. This work manifests that N_Q dopants provide principal catalytic activities of N-doped graphene.
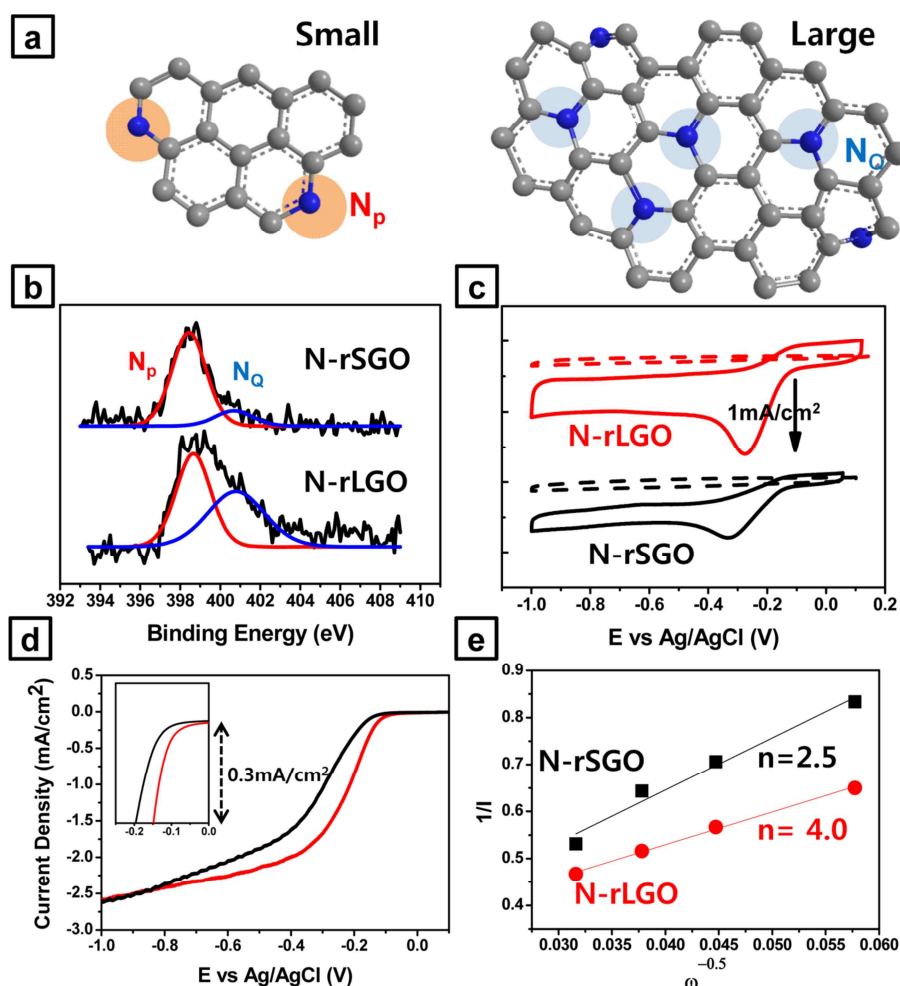

Figure 16. N-doped graphene and their ORR catalytic activity

5. Divalent Fe Atom Coordination in 2D Microporous Graphitic Carbon Nitride

Multiple metal-functionalized graphitic carbon nitride (g-C_3N_4) systems have been reported for versatile applications, but local coordination as well as its electronic structure variation upon incoming metal species is not well understood [41]. In this study, we investigated the bond coordination, electronic structure variation, and potential photocatalytic functionality enhancement of divalent Fe-coordinated g-C_3N_4 system (Fe-g-C_3N_4). Fe is chosen as targeting heteroatom species within the two-dimensional carbon nitride framework because of flexible oxidation states (II−IV), affinity toward the nitrogen-rich site, and presence of an analogous structural motif (e.g., Heme and Fe-NCNT) [42]. The synthesis of Fe-g-C_3N_4 is performed by thermal condensation reaction of dicyandiamide and divalent Fe chlorides precursors under nitrogen atmosphere (Figure 17(a)).
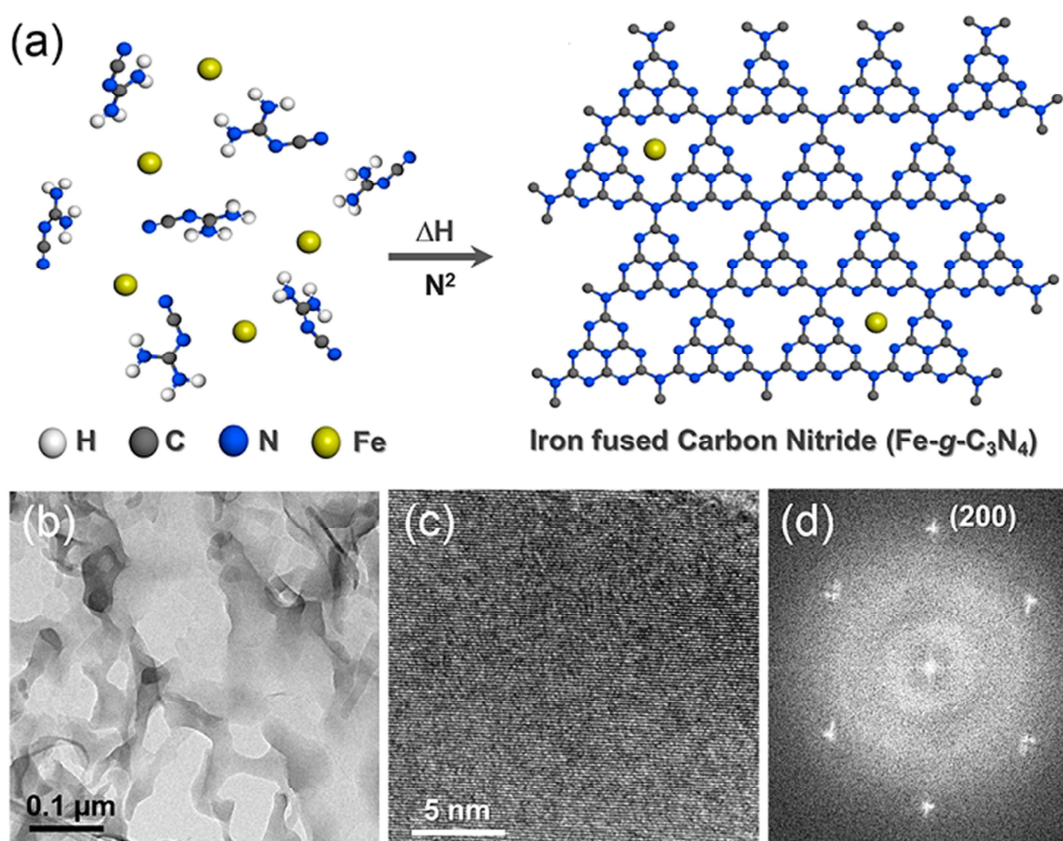

Figure 17. (a) Schematic representation of thermal condensation synthesis and proposed structure of divalent iron functionalized graphitic carbon nitride (Fe-g-C_3N_4). (b) Transmission electron microscope (TEM) images of Fe-g-C_3N_4 showing macroscopically disordered structure. (c) Well-defined local structure with (d) corresponding electron diffraction pattern of (200) orientation of graphitic carbon nitride phase.

Due to the absence of a structural directing agent, the macroscopic morphology of Fe-g-C_3N_4 (Figure 17(b)) is arbitrary and nonperiodic, but a high resolution view reveals its crystalline nature (Figure 17(c)). Fe-g-C_3N_4 shows a selected area electron diffraction (SAED) pattern that matches with the diffraction pattern of pristine g-C_3N_4 (Figure 17(d)). Throughout the specimens, both g-C_3N_4 and Fe-g-C_3N_4 show sporadic domains of well-defined polycrystalline regions as large as several tens of nanometers. This result indicates that the Fe

inclusion into carbon nitride structure does not distort the stacking of heptazine chain layers and that Fe-g-C_3N_4 likely retains the original crystal structure of graphitic carbon nitride. To obtain a microscopic understanding of how Fe atoms are incorporated within the carbon nitride matrix, solid-state NMR (ssNMR) technique was utilized as shown in Figure 18. Basic ssNMR measurements were conducted with magic angle spinning (MAS) technique to minimize anisotropic noise of solid state sample. In addition, cross-polarization magic angle spinning mode (vas) was monitored to detect hydrogen-coupled nuclei to distinguish the different types of carbon and nitrogen.
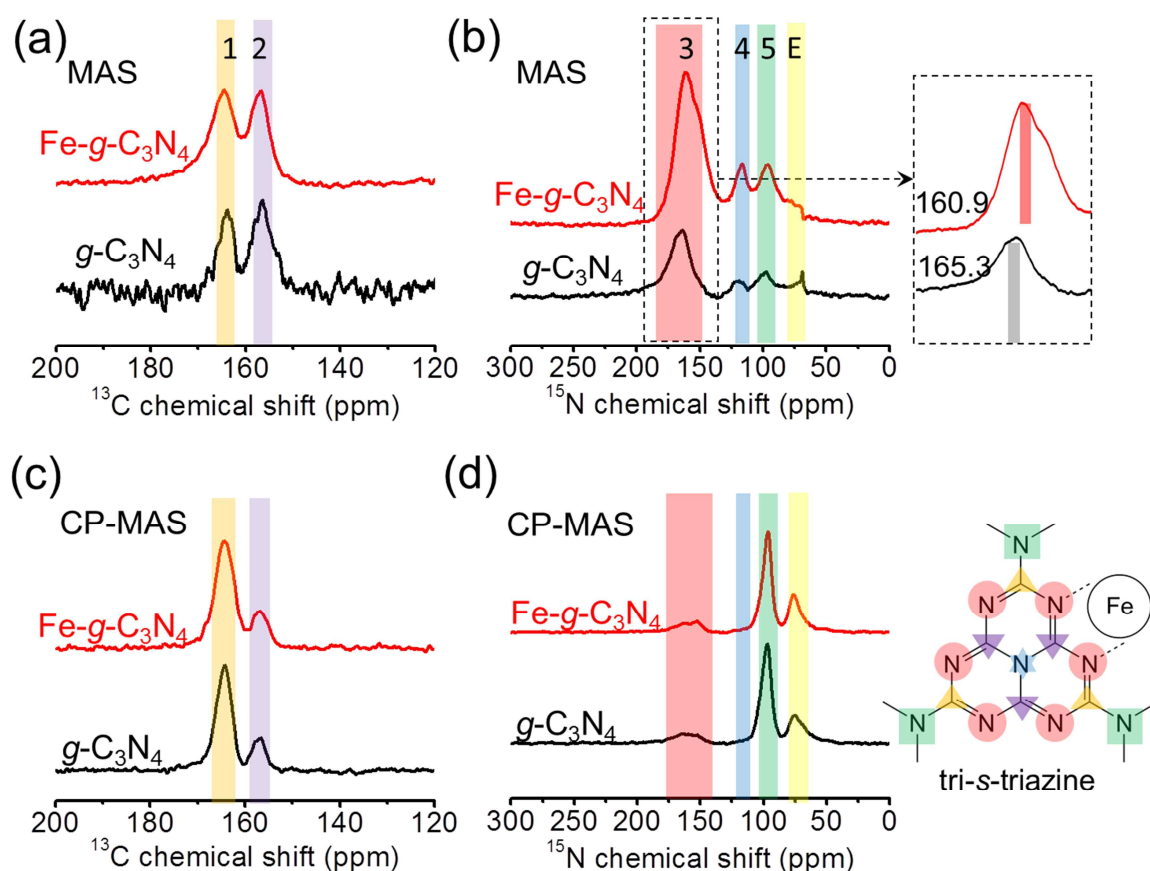

Figure 18. Magic angle spinning solid-state nuclear magnetic resonance spectroscopy (MAS ssNMR) of g-C_3N_4 and Fe- g-C_3N_4 in (a) 13C nucleus and (b) 15N nucleus. MAS ssNMR with cross-polarization (CP-MAS) setup for both samples in (c) 13C nucleus and (d) 15N nucleus. In these spectra, peaks 1 (orange triangle), 2 (purple reverse triangle), 3 (red circle), 4 (blue star), 5 (green square), and E correspond to outer carbon, inner carbon, intermediate position nitrogen, tertiary central nitrogen, terminal nitrogen, and edge nitrogen in tri-s-triazine unit, respectively

Graphitic carbon nitride is composed of continuous chains of heptazine units (Figure 18(a)), where two types of carbon (3 outer and 3 inner position) and three types of nitrogen (1 central, 6 intermediate, and 1 terminal position) exist. MAS NMR confirms the stoichiometric ratios of both pristine and Fe-functionalized carbon nitride. Based on the assumption that Fe binds to these intermediate nitrogen, lone pair electrons of nitrogen may share electrons with divalent Fe through empty d-orbitals, which will result in reduced electron negativity and chemical shift as shown in Figure 18(b). The stoichiometric ratio of intermediate (peak 3), central (peak 4), and terminal (peak 5) nitrogen in carbon nitride is 6:1:1. MAS 15N NMR intensities of peaks 3−5 represent well the numbers of corresponding types of nitrogen. CP-

MAS NMR spectroscopy provides additional information about the local positions of carbon and nitrogen (Figure 18(c-d)) which confirms that Fe is positioned at the center of pores created by buckling of tri-s-triazine units, coordinated by edge side of nitrogen.

To demonstrate Fe inclusion effect on the carbon nitride scaffold, optical absorption and photocatalytic behaviors of the as-prepared pure g-C_3N_4 and Fe-g-C_3N_4 are compared, as presented in Figure 19. Fe-g-C_3N_4 exhibits enhanced absorption at the UV-vis range compared with pristine g-C_3N_4 under the same spectroscopic configuration (Figure 19(a)). The photocatalytic activities of the synthesized g-C_3N_4 and Fe-g-C_3N_4 were evaluated for the degradation of *p*-nitrophenol (PNP) under sunlight irradiation (Figure 19(b)). The pristine and Fe-g-C_3N_4 decompose PNP by 27% and 55% within 5 hr, respectively, indicating that the photocatalytic activity is significantly promoted by Fe doping. This result reflects divalent Fe acting as the electron- and hole-trapping site, resulting in enhanced separation of photogenerated excitons and interfacial electron transfer process.
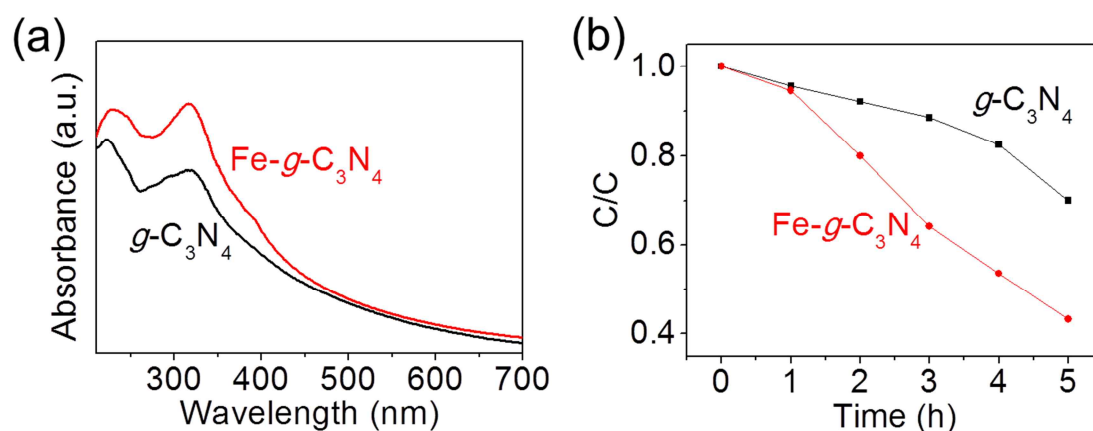

Figure 19. (a) UV−vis absorption spectra. (b) Photocatalytic activity of PNP degradation in aqueous solution under solar irradiation of g-C_3N_4 and Fe- g-C_3N_4.

References

[1]   K. S. Novoselov, V. I. Fal'ko, L. Colombo, P. R. Gellert, M. G. Schwab, K. Kim, *Nature* **2012**, *490*, 192-200.
[2]   L. Britnell, R. V. Gorbachev, R. Jalil, B. D. Belle, F. Schedin, A. Mishchenko, T. Georgiou, M. I. Katsnelson, L. Eaves, S. V. Morozov, N. M. R. Peres, J. Leist, A. K. Geim, K. S. Novoselov, L. A. Ponomarenko, *Science* **2012**, *335*, 947-950.
[3]   S. Yang, Y. Gong, J. Zhang, L. Zhan, L. Ma, Z. Fang, R. Vajtai, X. Wang, P. M. Ajayan, *Adv. Mater.* **2013**, *25*, 2452-2456.
[4]   Z. Liu, L. Song, S. Z. Zhao, J. Q. Huang, L. L. Ma, J. N. Zhang, J. Lou, P. M. Ajayan, . *Nano Lett.* **2011**, *11*, 2032-2037.
[5]   J. L. Gunjakar, I. Y. Kim, J. M. Lee, N. S. Lee, S. J. Hwang, *Energ. Environ. Sci.* **2013**, *6*, 1008-1017.
[6]   S. H. Lee, D. H. Lee, W. J. Lee, S. O. Kim, *Adv. Funct. Mater,* **2011**, *21*, 1338-1354.
[7]   H. Chen, M. B. Muller, K. J. Gilmore, G. G. Wallace, D. Li, *Adv. Mater.* **2008**, *20*, 3557-3561.

[8]   D. Li, M. B. Muller, S. Gilje, R. B. Kaner, G. G. Wallace, *Nat. Nanotechnol.* **2008**, *3*, 101-105.

[9]   Z. Xu, C. Gao, *Nature Commun.* **2011**, *2*, 571

[10]   J. Y. Luo, J. Kim, J. X. Huang, *Acc. Chem. Res.* **2013**, *46*, 2225-2234.

[11]   Y. X. Xu, K. X. Sheng, C. Li, G. Q. Shi, *ACS Nano* **2010**, *4*, 4324-4330.

[12]   X. W. Yang, J. W. Zhu, L. Qiu, D. Li, *Adv. Mater.* **2011**, *23*, 2833-2838.

[13]   Y. Zhao, J. Liu, Y. Hu, H. H. Cheng, C. G. Hu, C. C. Jiang, L. Jiang, A. Y. Cao, L. T. Qu, *Adv. Mater.* **2013**, *25*, 591-595.

[14]   P. I. Järvinen, S. K. Hämäläinen, K. Banerjee, P. Häkkinen, M. Ijäs, A. Harju, P. Liljeroth, *Nano Lett.* **2013**, *13*, 3199-3204.

[15]   D. Bléger, F. Mathevet, D. Kreher, A. J. Attias, A. Bocheux, S. Latil, L. Douillard, C. Fiorini-Debuisschert, F. Charra, *Angew. Chem. Int. Ed.* **2011**, *50*, 6562-6566.

[16]   P. Du, M. Jaouen, A. Bocheux, C. Bourgogne, Z. Han, V. Bouchiat, D. Kreher, F. Mathevet, C. Fiorini-Debuisschert, F. Charra, *Angew. Chem.* **2014**, *126*, 10224-10230.

[17]   K. Parvez, Z.-S. Wu, R. Li, X. Liu, R. Graf, X. Feng, K. Müllen, *J. Am. Chem. Soc.* **2014**, *136*, 6083-6091.

[18]   W. K. Bae, K. Char, H. Hur, S. Lee, *Chem. Mater.* **2008**, 20, 531-539.

[19]   B. I. Ipe, K. G. Thomas, S. Barazzouk, S. Hotchandani, P. V. Kamat, *J. Phys.Chem. B* **2002**, *106*, 18-21.

[20]   G. Battistini, P. G. Cozzi, J.-P. Jalkanen, M. Montalti, L. Prodi, N. Zaccheroni, F. Zerbetto, *ACS Nano* **2008**, *2*, 77-84.

[21]   X. Peng, J. A. Misewich, S. S. Wong, M. Y. Sfeir, *Nano Lett.* **2011**, *11*, 4562-4568.

[22]   W. J. Yu, Z. Li, H. Zhou, Y. Chen, Y. Wang, Y. Huang, X. Duan, *Nat. Mater.* **2013**, *12*, 246-252.

[23]   H. Fang, C. Battaglia, C. Carraro, S. Nemsak, B. Ozdol, J. S. Kang, H. A. Bechtel, S. B. Desai, F. Kronast, A. A. Unal, *Proc. Nat. Acad. Sci.* **2014**, *111*, 6198-6202.

[24]   Y. Oh, V.-D. Le, U. N. Maiti, J. O. Hwang, W. J. Park, J. Lim, K. E. Lee, Y.-S. Bae, Y.-H. Kim, S. O. Kim, *ACS Nano* **2015**, *9*, 9148-9157.

[25]   R. T. Yang, *Adsorbents: Fundamentals and Applications*, John Wiley & Sons, **2003**.

[26]   S. U. Rege, R. T. Yang, *Sep. Sci. Technol.* **2001**, *36*, 3355-3365.

[27]   P. D. Dietzel, V. Besikiotis, R. Blom, *J. Mater. Chem.* **2009**, *19*, 7362-7370.

[28]   Y. S. Bae, R. Q. Snurr, *Angew. Chem. Int. Ed.* **2011**, *50*, 11586-11596.

[29]   R. Banerjee, H. Furukawa, D. Britt, C. Knobler, M. O'Keeffe, O. M. Yaghi, *J. Am. Chem. Soc.* **2009**, *131*, 3875-3877.

[30]   J.-H. Park, J.-N. Kim, S.-H. Cho, J.-D. Kim, R. T. Yang, *Chem. Eng. Sci.* **1998**, *53*, 3951-3963.

[31]   P. Kumar, U. N. Maiti, K. E. Lee, S. O. Kim, *Carbon* **2014**, *80*, 453-461.

[32]   S. H. Aboutalebi, M. M. Gudarzi, Q. B. Zheng, J. K. Kim, *Adv. Funct. Mater.* **2011**, *21*, 2978-2988.

[33]   L. Onsager, *Ann. N.Y. Acad. Sci.* **1949**, *51*, 627-659.

[34]   R. B. Bird, R. Armstrong, O. Hassager, *"Dynamics of Polymeric Liquids (2nd Ed.)"*, Wiley, New York, **1987**.

[35]   R. I. Tanner, *Engineering Rheology, Vol. 52*, OUP Oxford, **2000**.

[36]   J. F. Douglas, *Macromolecules* **1992**, *25*, 1468-1474.

[37]   M. A. Bates, D. Frenkel, *J. Chem. Phys.* **1999**, *110*, 6553-6559

[38]   J. E. Kim, T. H. Han, S. H. Lee, J. Y. Kim, C. W. Ahn, J. M. Yun, S. O. Kim, *Angew. Chem. Int. Ed.* **2011**, *50*, 3043-3047.

[39]   K. E. Lee, J. E. Kim, U. N. Maiti, J. Lim, J. O. Hwang, J. Shim, J. J. Oh, T. Yun, S. O. Kim, *ACS Nano* **2014**, *8*, 9073-9080.

[40] L. Qu, Y. Liu, J.-B. Baek, L. Dai, *ACS Nano* **2010**, *4*, 1321-1326.
[41]   X.-H. Li, M. Antonietti, *Chem. Soc. Rev.* **2013**, *42*, 6593-6604.
[42] Y. Oh, J. O. Hwang, E.-S. Lee, M. Yoon, V.-D. Le, Y.-H. Kim, D. H. Kim, S. O. Kim, *ACS Appl. Mater. & Inter.* **2016**, *8*, 25438-25443.

List of Publications and Significant Collaboration by AOARD Supported Project

a) Papers Published in Peer-reviewed Journals

1. K. E. Lee, J. E. Kim, U. N. Maiti, J. Lim, J. O. Hwang, J. Shim, J. J. Oh, T. Yun, S. O.Kim, *ACS Nano* **2014**, *8*, 9073-9080.
2. P. Kumar, U. N. Maiti, K. E. Lee, S. O. Kim, *Carbon* **2014**, *80*, 453-461.
3. Y. Oh, V.-D. Le, U. N. Maiti, J. O. Hwang, W. J. Park, J. Lim, K. E. Lee, Y.-S. Bae, Y.-H. Kim, S.O. Kim, *ACS Nano* **2015**, *9*, 9148-9157.
4. Y. Oh, J. O. Hwang, K-S. Lee, M. Yoon, V.-D. Le, Y.-H. Kim, D. H. Kim, S. O. Kim, *ACS Appl. Mater. Interfaces* **2016**, *8*, 25438-25443.

b) Conference Presentations

1. S. O. Kim, "Graphitic Carbon Assembly and Modification for Optimum Nanomaterial and Device Applications", The 5th A3 (Asian3) Symposium on Emerging Materials: sp2 *Nanocarbon for Energy, Tianjin, China, October 18-22, 2014. (Invited Presentation)*
2. K.-S. Lee, S.-M. Jeon, J. Jung, X.-C. Teng, *"Charge and Energy Transfer Properties of Quantum Dot-Based Organic-Inorganic Hybrid Materials"*, International Workshop on Nano and Bio-Photonics, Cabourg, France, Dec. 6-11, 2015. (Invited Presentation)
3. S. O. Kim, *"Chemically Modified Carbon Nanotubes and Graphene: Synthesis, Assembly and Applications"* 2015 The International Chemical Congress of Pacific Basin Society (PacifiChem 2015), Honolulu, USA, December 15-20, 2015. (Invited Presentation)
4. S. H. Kim, J. Jung, X.-C. Teng, P. Prabhakaran, K.-S. Lee, *"Novel Organic-Inorganic Hybrids with Magnetic, Magneto-Optic and Optoelectronic Functions"*, Sorbonne-UPMC, Paris, France, July 5-8, 2016.
5. S. O. Kim, "Directed Nanoscale Assembly of Graphene Based Materials", American Physical Society (APS) March Meeting, Baltimore, USA, March 14-18, 2016. (Invited Presentation)
6. S. O. Kim, *"Graphene Based Hybrid Nanostructures: Nanoscale Assembly and Chemical Modification"*, 40th International Conference and Exposition on Advanced Ceramics and Composites (ICACC2016), Florida, USA, January 24-29, 2016. (Invited Presentation)
7. K.-S. Lee, S.-H. Kim, J. Jung, X.-C. Teng, P. Prabhakaran, K.-S. Lee, "*Graphene-Based Organic-Inorganic Hybrids with Optoelectronic and Magneto-Optic Functions*", SPIE-Photonics West 2017, San Francisco, Jan. 28-Feb. 2, 2017. (Invited Lecture)
8. S.-H. Kim, E.-B. Jung, X.-C. Teng, P. Prabhakaran, K.-S. Lee, "*Graphene/Quantum Dot-Based Self-Assembled Structures*", Winter Meeting of Optical Sciety of Korea, High1 Resort, Gangwon-do, Korea, Feb. 15-17, 2017.
9. J. Jung, K.-S. Lee, E.-B. Jung, X.-C. Teng, S.-H. Kim, P. Prabhakaran, K.-S. Lee, "*Quantum Dots Self-Assembly on Graphne Surface via π- π Interaction*", Spring Meeting of the Polymer Sciety of Korea, Daejeon, Korea, April 5-7, 2017.

10. S. O. Kim, *"Nanoscale Assembly and Chemical Modification of Graphene Based Nanomaterials: Graphene Oxide Liquid Crystals and Other Relevant Nanostructures"*, Graphene 2017, Barcelona, Spain, March 28-31, 2017. (Invited Presentation)

d) Manuscripts under Preparation

1. S.P. Sasikala, P. Prabhakaran, S. Y. Kim, J. Jung, S. O. Kim and K.-S. Lee, "Solution processed 2D-2D van der Waals Heterostructures of Graphene andTungsten Diselenide", *to be submitted* 2017.
2. S.Y. Kim, J. Y. Jung, S P. Sasikala, S.O. Kim, P. Prabhakaran, K.-S. Lee, "Solution Processed 0D-2D Van der Waals Heterostructures of Graphene and CdSe QDs", *to be submitted* 2017.

e) Significant Collaborations

The expertise from both the PI's groups was combined for the works listed as under preparation. The self-assembly experiments of 0D-2D materials were carried out in Hannam university using graphene provided by the group in KAIST. The characterization, study of properties of the nanohybrid materials and their applications were done at Hannam University. Similarly 2D-2D heterostructures were assembled in KAIST with ligands provided from Hannam Univeristy, the characterization study of properties of the nanohybrid materials and their applications are being carried out in KAIST.